Draft version November 29, 2018
Typeset using LaTeX **twocolumn** style in AASTeX62

Binary Black Hole Population Properties Inferred from the First and Second Observing Runs of Advanced LIGO and Advanced Virgo

The LIGO Scientific Collaboration and The Virgo Collaboration

ABSTRACT

We present results on the mass, spin, and redshift distributions of the ten binary black hole mergers detected in Advanced LIGO's and Advanced Virgo's first and second observing runs. We constrain properties of the binary black hole (BBH) mass spectrum using models with a range of parameterizations of the BBH mass and spin distributions. We find that the mass distribution of the more massive black hole in each binary is well approximated by models with almost no black holes larger than 45 $M_{\odot}$, and a power law index of $\alpha = 1.6^{+1.5}_{-1.7}$ (90% credibility). We also show that BBHs are unlikely to be composed of black holes with large spins aligned to the orbital angular momentum. Modelling the evolution of the BBH merger rate with redshift, we show that it is increasing with redshift with credibility 0.88. Marginalizing over uncertainties in the BBH population, we find robust estimates of the BBH merger rate density of $R = 52.9^{+55.6}_{-27.0}$ Gpc^{-3} yr^{-1}(90% credibility). As the BBH catalog grows in future observing runs, we expect that uncertainties in the population model parameters will shrink, potentially providing insights into the formation of black holes via supernovae, binary interactions of massive stars, stellar cluster dynamics, and the formation history of black holes across cosmic time.

1. INTRODUCTION

The second LIGO/Virgo observing run (O2) spanned nine months between November 2016 through August 2017, building upon the first, four-month run (O1) in 2015. The LIGO/Virgo gravitational-wave (GW) interferometer network is comprised of two instruments in the United States (LIGO) (Harry & LIGO Scientific Collaboration 2010; Abbott et al. 2016a) and a third in Europe (Virgo) (Acernese et al. 2015), the latter joining the run in the summer of 2017. In total, ten binary black hole (BBH) mergers have been detected to date (Abbott et al. 2018). These observations constrain the volumetric BBH merger rate to $\mathcal{R}_{\rm BBH} \in [9.7, 101]$ Gpc^{-3} yr^{-1} (Abbott et al. 2018) after accounting for 0.46 yr of observational time in O1 and O2. The BBHs detected possess a wide range of physical properties. The lightest so far is GW170608 (Abbott et al. 2017a) with an inferred total mass of $18.7^{+3.3}_{-0.7} M_{\odot}$. GW170729 (Abbott et al. 2018)—exceptional in several ways—is likely to be the heaviest BBH to date, having total mass $85.2^{+15.4}_{-11.2} M_{\odot}$, as well as the most distant, at redshift $0.48^{+0.19}_{-0.20}$. GW151226 was the first observation to show evidence for at least one black hole with a spin greater than zero (Abbott et al. 2016b).

By measuring the distributions of mass, spin, and merger redshift in the BBH population, we may make inferences about the physics of binary mergers and better understand the origin of these systems. We employ Bayesian inference and modelling (Gelman et al. 2004; Mandel 2010; Foreman-Mackey et al. 2014) which, when applied to parameterized models of the population, is able to infer population-level parameters — sometimes called hyperparameters to distinguish them from the event-level parameters — while properly accounting for the uncertainty in the measurements of each event's parameters (Mandel 2010; Hogg et al. 2010).

The structure and parameterization of BBH populations models are guided by the physical processes and evolutionary environments in which BBH are expected to form and merge. Several BBH formation channels have been proposed in the literature, each of them involving a specific environment and a number of physical processes. For example, BBHs might form from isolated massive binaries in the galactic field through common-envelope evolution (Bethe & Brown 1998; Portegies Zwart & Yungelson 1998; Belczynski et al. 2002; Voss & Tauris 2003; Dewi et al. 2006; Belczynski et al. 2007, 2008; Dominik et al. 2013; Belczynski et al. 2014; Mennekens & Vanbeveren 2014; Spera et al. 2015; Tauris et al. 2017; Eldridge & Stanway 2016; Stevenson et al. 2017b; Chruslinska et al. 2018; Mapelli et al. 2017; Giacobbo et al. 2018; Mapelli & Giacobbo 2018; Kruckow et al. 2018; Giacobbo & Mapelli 2018) or via chemically homogeneous evolution (Marchant et al. 2016; de Mink & Mandel 2016; Mandel & de Mink 2016). Alternatively, BBHs might form via dynamical processes in stellar clusters (Portegies Zwart & McMillan 2000; Kulkarni et al. 1993; Sigurdsson & Hernquist 1993; Grindlay et al. 2006;

O'Leary et al. 2006; Sadowski et al. 2008; Ivanova et al. 2008; Downing et al. 2010, 2011; Clausen et al. 2013; Ziosi et al. 2014; Rodriguez et al. 2015, 2016a; Mapelli 2016; Askar et al. 2017; Banerjee 2017; Chatterjee et al. 2017) and galactic nuclei (Antonini & Perets 2012; Antonini & Rasio 2016; Petrovich & Antonini 2017), evolution of hierarchical triple systems (Antonini et al. 2014; Kimpson et al. 2016; Antonini et al. 2017), gas drag and stellar scattering in accretion disks surrounding supermassive black holes (McKernan et al. 2012; Bartos et al. 2017; Stone et al. 2017). Finally, BBHs might originate as part of a primordial black hole population in the early Universe (Carr & Hawking 1974; Carr et al. 2016; Sasaki et al. 2016; Inomata et al. 2017; Inayoshi et al. 2016; Bird et al. 2016; Ali-Haïmoud et al. 2017; Chen & Huang 2018; Ando et al. 2018). Each channel contributes differently to the distributions of the mass, spin, distance, and orbital characteristics of BBHs.

There are several processes common to most pathways through stellar evolution which affect the properties of the resultant BBH system. Examples include mass loss (Vink et al. 2001; Vink & de Koter 2005; Gräfener & Hamann 2008) and supernova (O'Connor & Ott 2011; Fryer et al. 2012; Janka 2012; Ugliano et al. 2012; Ertl et al. 2016; Sukhbold et al. 2016). The mass of the compact object left after the supernova is directly related to its pre-supernova mass and the supernova mechanism itself. Metallicity has been shown (Kudritzki & Puls 2000; Vink et al. 2001) to have dramatic effects on stellar mass loss through winds — line-driven winds are quenched in metal-poor progenitors, enabling large black holes to form through direct collapse or post-supernova mass fallback (Heger et al. 2003; Mapelli et al. 2009; Belczynski et al. 2010; Spera et al. 2015). This also, in turn, might suppress supernova kicks (Fryer et al. 2012) and hence enhance the number of binaries which are not disrupted.

Theoretical and phenomenological models of BBH formation are explored by population synthesis. This requires modelling not only of stellar evolution but also the influence of their evolutionary environments. For instance, isolated evolution in galactic fields requires prescriptions for binary interactions, such as common envelope physics (De Marco et al. 2011; Ivanova et al. 2013), as well as mass transfer episodes (Dosopoulou & Kalogera 2016). Meanwhile, BBH formation in dense stellar clusters (Ziosi et al. 2014; Rodriguez et al. 2015, 2016a; Mapelli 2016; Askar et al. 2017; Banerjee 2017) is impacted primarily by dynamical interactions within the cluster (Fregeau 2004; Morscher et al. 2013), but also by cluster size and initial mass functions (Scheepmaker et al. 2007; Portegies Zwart et al. 2010; Kremer et al. 2018). GW observations provide an alternative to sharpen our understanding of those processes.

Electromagnetic observations and modeling of systems containing black holes have led to speculation about the existence of a pair of gaps in the black hole mass spectrum. Both gaps may be probed using data from current ground-based gravitational-wave interferometers, and as such, have been the target of parametric studies. At low masses, observations of X-ray binaries (XRB) combined via Bayesian population modeling (Bailyn et al. 1998; Özel et al. 2010; Farr et al. 2011b) suggest a minimum black hole mass well above the largest neutron star masses. While the existence and nature of this gap is still uncertain (Kreidberg et al. 2012), it is proposed to exist between the most massive neutron stars (Özel & Freire 2016; Freire et al. 2008; Margalit & Metzger 2017) ($2.1-2.5 M_\odot$) and the lightest black holes $\sim 5 M_\odot$. It is possible to constrain the existence of this lower mass gap with GW observations (Littenberg et al. 2015; Kovetz et al. 2017; Mandel et al. 2017). In Section 3, we find our current GW observations do not inform the upper edge of this gap, inferring a minimum mass on the primary black hole at $m_{\rm min} \lesssim 9$ $M_\odot$. Our volumetric sensitivity to BBH systems with masses less than 5 $M_\odot$ is small enough that we expect (and observe) no events in the lower gap region. Thus, our ability to place constraints in this region is severely limited.

Recently, there have been claims of an upper cutoff in the BBH mass spectrum based on the first few LIGO detections (Fishbach & Holz 2017; Talbot & Thrane 2018; Wysocki et al. 2018; Roulet & Zaldarriaga 2018; Bai et al. 2018). This might be expected as a consequence of a different supernova type, called the (pulsational) pair-instability supernova (Heger & Woosley 2002; Belczynski et al. 2016b; Woosley 2017; Spera & Mapelli 2017; Marchant et al. 2018). This process leaves no black hole remnants between $\sim 50 - 150 M_\odot$, because the progenitor star is partially or entirely disrupted by the explosion. Pulsational pair-instability supernovae may also contribute a build-up of black holes near the lower edge of the gap. Consistent with prior work, we find that all our mass models have almost no merging black holes above ~ 45 $M_\odot$. We also find mild evidence ($\ln \mathrm{BF} = -1.40$) against a pure power-law model, which might be the result of a build up at the heavy end of the mass spectrum.

Black hole spin measurements also provide a powerful tool to discriminate between different channels of BBH formation (Mandel & O'Shaughnessy 2010; Abbott et al. 2016c; Vitale et al. 2017; Farr et al. 2017, 2018). For example, BBHs formed in a dynamic environment will have no preferred direction for alignment, producing isotropically oriented spins (Sigurdsson & Hernquist 1993; Portegies Zwart & McMillan 2000; Mandel & O'Shaughnessy 2010; Rodriguez et al. 2015, 2016c; Stone et al. 2017). By contrast, isolated binaries are expected to preferentially produce mergers with alignment between the spins of the constituent black holes and the orbital angular momentum of the system (Tutukov & Yungelson 1993; Kalogera 2000; Grandclément et al. 2004; Belczynski et al. 2016a; Rodriguez et al. 2016c; Mandel & de Mink 2016; Marchant et al. 2016; Stevenson et al. 2017b; O'Shaughnessy et al. 2017; Gerosa et al. 2018). Other effects occurring in stellar systems like hierarchical triples could also produce a weak preference for certain spin-orbit misalignments (Rodriguez & Antonini 2018). All of our parameterized models point to preferences for low spin magnitudes. In Section 5, we find that the dimensionless spin magnitude distribution prefers distributions which decline as the spin magnitude increases from zero, but our ability to distinguish between assumed distributions of spin orientation is very limited.

Observational constraints on the BBH merger rate (Abbott et al. 2016d; Abbott et al. 2018) generally assume a rate density which is uniform in the comoving volume. As first shown in Fishbach et al. (2018), it is also possible to search for redshift evolution in the rate density using current data. Different redshift-dependent evolutionary behavior is possible (Dominik et al. 2013; Mandel & de Mink 2016; Rodriguez et al. 2016a; Mapelli et al. 2017; Rodriguez & Loeb 2018) with different environments and stellar evolution scenarios (Belczynski et al. 2016a). For instance, theoretical models of isolated evolution employ a distribution of times to merger $p(t_{\rm GW}) \propto t_{\rm GW}^{-1}$ (Dominik et al. 2012; Belczynski et al. 2016a). Due to the short lifetimes of massive stars, this implies many isolated binaries will coalesce near their formation redshift. This would produce a BBH merger rate that approximately tracks the star formation rate, peaking near $z \sim 2$. We find in Section 4 that the current sample of BBH mergers does not provide enough information to confidently constrain anything but the most extreme models. While we place more posterior mass on merger rates that increase with increasing redshift than those that decrease, the scenario of a uniform rate in comoving volume is comfortably within our constraints.

GW170817, the first binary neutron star merger observed through GW emission (Abbott et al. 2017b), was detected by GW observatories and associated with a short GRB (Abbott et al. 2017c)) in August of 2017. A subsequent post-merger transient (AT 2017gfo) was observed across the electromagnetic spectrum, from radio (Alexander et al. 2017), NIR/optical (Coulter et al. 2017; Soares-Santos et al. 2017; Chornock et al. 2017; Cowperthwaite et al. 2017; Nicholl et al. 2017; Pian et al. 2017), to X-ray (Troja et al. 2017; Margutti et al. 2017) and γ-ray (Abbott et al. 2017c; Goldstein et al. 2017; Savchenko et al. 2017). Unfortunately, with only one confident detection, it is not yet possible to infer details of binary neutron star populations more than to note that the gravitational-wave measurement is mostly compatible with the observed Galactic population (Özel et al. 2012). However, if GW170817 did form a black hole, it would also occupy the lower mass gap described previously.

We structure the paper as follows. First, notation and models are established in Section 2. Section 3 describes our modeling of the black hole mass distribution, followed by rate distributions and evolution in Section 4. The black hole spin magnitude and orientation distributions are discussed in Section 5. We conclude in Section 6. Studies of various systematics are presented in Appendix A. In Appendix B we present additional studies of spin distributions with model selection for a number of zero-parameter spin models and mixtures of spin orientations. To motivate and enable more detailed studies, we have established a repository of our samples and other derived products[1].

2. DATA, NOTATION, AND MODELS

In this work, we analyze the population of 10 BBH merger events confidently identified in the first and second observing run (O1 and O2) (Abbott et al. 2018). We do not include marginal detections, but these likely have a minimal impact our conclusions here (Gaebel et al. 2018). Ordered roughly from smallest to most massive by source-frame chirp mass, the mergers considered in this paper are GW170608, GW151226, GW151012, GW170104, GW170814, GW170809, GW170818, GW150914, GW170823, and GW170729.

The individual properties of those 10 sources were inferred using a Bayesian framework, with results summarized in Abbott et al. (2018). For BBH systems, two waveform models have been used, both calibrated to numerical relativity simulations and incorporating spin effects, albeit differently: `IMRPhenomPv2` (Hannam et al. 2014; Husa et al. 2016; Khan et al. 2016), which includes an effective representation of precession effects, and `SEOBNRv3` (Pan et al. 2014; Taracchini et al. 2014; Babak et al. 2017), which incorporates all spin degrees

[1] The data release for this work can be found at https://dcc.ligo.org/LIGO-P1800324/public.

of freedom. The results presented in this work use IMRPhenomPv2; a discussion of potential systematic biases in our inference are discussed in Appendix A. We also refer to Appendix B in (Abbott et al. 2018) for more details on comparisons between those two waveform families.

To assess the stability of our results to statistical effects and systematic error we focus on one modestly exceptional event. Both GW151226 and GW170729 exhibit evidence for measurable black hole spin, but GW170729 in particular is an outlier by several other metrics as well. In addition to spins, it is also more massive and more distant than any of the other events in the catalog. All events used in the population analysis have confident probabilities of astrophysical origin, but GW170729 is the least significant, having the smallest odds ratio of astrophysical versus noise origin (Abbott et al. 2018). As we describe in Sections 3 and 4, this event has an impact on our inferred merger rate versus both mass and redshift. To demonstrate the robustness of our result, we present these analyses twice: once using every event, and again omitting GW170729.

2.1. *Binary Parameters*

A coalescing compact binary in a quasi-circular orbit can be completely characterized by its eight intrinsic parameters, namely its component masses m_i and spins $\boldsymbol{S}_i$, and its seven extrinsic parameters: right ascension, declination, luminosity distance, coalescence time, and three Euler angles characterizing its orientation (e.g., inclination, orbital phase, and polarization). While binary eccentricity is also a potentially observable quantity in BBH mergers, our ability to parameterize (Huerta et al. 2014, 2017; Klein et al. 2018; Hinder et al. 2018) and measure (Coughlin et al. 2015; Abbott et al. 2016c, 2017d; Lower et al. 2018) eccentricity is an area of active development. For low to moderate eccentricity at formation, binaries are expected to circularize (Peters 1964; Hinder et al. 2008) before entering the bandwidth of ground-based GW interferometers. We therefore assume zero eccentricity in our models.

In this work, we define the mass ratio as $q = m_2/m_1$ where $m_1 \geq m_2$. The frequency of gravitational wave emission is directly related to the component masses. However, due to the expansion of spacetime as the gravitational wave is propagating, the frequencies measured by the instrument are redshifted relative to those emitted at the source (Thorne 1983). We capture these effects by distinguishing between masses as they would be measured in the source frame, denoted as above, and the redshifted masses, $(1+z)m_i$, which are measured in the detector frame. Meanwhile, the amplitude of the wave scales inversely with the luminosity distance (Misner et al. 1973). We use the GW measurement of the luminosity distance to obtain the cosmological redshift and therefore convert between detector-frame and source-frame masses. We assume a fixed Planck 2015 (Planck Collaboration et al. 2016) cosmology throughout to convert between a source's luminosity distance and its redshift (Hogg 1999).

We characterize black hole spins using the dimensionless spin parameter $\boldsymbol{\chi}_i = \boldsymbol{S}_i/m_i^2$. Of particular interest are the magnitude of the dimensionless spin, $a_i = |\boldsymbol{\chi}_i|$, and the tilt angle with respect to the orbital angular momentum, $\hat{\boldsymbol{L}}$, given by $\cos t_i = \hat{\boldsymbol{L}} \cdot \hat{\boldsymbol{\chi}}_i$. We also define an overall effective spin, $\chi_{\rm eff}$ (Damour 2001; Racine 2008; Ajith et al. 2011), which is a combination of the individual spin components along to orbital angular momentum:

$$\chi_{\rm eff} = \frac{(\boldsymbol{\chi}_1 + q\boldsymbol{\chi}_2)\cdot\hat{\boldsymbol{L}}}{1+q}. \tag{1}$$

$\chi_{\rm eff}$ is approximately proportional to the lowest order contribution to the GW waveform phase that contains spin for systems with similar masses. Additionally, $\chi_{\rm eff}$ is conserved throughout the binary evolution to high accuracy (Racine 2008; Gerosa et al. 2015).

2.2. *Model Features*

To present general results, and to allow us to vary small subsets of parameters influencing the mass and spin distributions while leaving others fixed, we adopt the union of the parameterizations presented in Talbot & Thrane (2017); Fishbach & Holz (2017); Wysocki et al. (2018); Talbot & Thrane (2018); Fishbach et al. (2018). The general model family has one parameter describing the local merger rate, $\mathcal{R}_0$; **8** parameters to characterize the mass model; **3** to characterize each black hole's spin distribution; and one parameter characterizing redshift dependence. We refer to the set of these population parameters as θ. All of the population parameters introduced in this section are summarised in Table 1.

2.3. *Parameterized Mass Models*

The power-law distribution considered previously (Abbott et al. 2016d, 2017e) modeled the BBH primary mass distribution as a one-parameter power-law, with fixed limits on the minimum and maximum allowed black hole mass. With our sample of ten binaries, we extend this analysis by considering three increasingly complex models for the distribution of black hole masses. The first extension, Model A (derived from Fishbach & Holz (2017); Wysocki et al. (2018)), allows the maximum black hole mass $m_{\max}$ and the power-law index α to

α	Spectral index of m_1 for the power-law distributed component of the mass spectrum.
$m_{\rm max}$	Maximum mass of the power-law distributed component of the mass spectrum.
$m_{\rm min}$	Minimum black hole mass.
β_q	Spectral index of the mass ratio distribution.
λ_m	Fraction of binary black holes in the Gaussian component.
μ_m	Mean mass of black holes in the Gaussian component.
σ_m	Standard deviation of masses of black holes in the Gaussian component.
δm	Mass range over which black hole mass spectrum turns on.
ζ	Fraction of binaries with isotropic spin orientations.
σ_i	Width of the preferentially aligned component of the distribution of black hole spin orientations.
$\mathbb{E}[a]$	Mean of the Beta distribution of spin magnitudes.
$\text{Var}[a]$	Variance of the Beta distribution of spin magnitudes.
λ	How the merger rate evolves with redshift.

Table 1. Parameters describing the binary black hole population. See the text for a more thorough discussion and the functional forms of the models.

vary. In Model B (derived from Kovetz et al. (2017); Fishbach & Holz (2017); Talbot & Thrane (2018)) the minimum black hole mass $m_{\rm min}$ and the mass ratio power-law index β_q are also free parameters. Explicitly, the mass distribution in Model A and Model B takes the form

$$p(m_1, m_2|m_{\rm min}, m_{\rm max}, \alpha, \beta_q) \propto \begin{cases} C(m_1) m_1^{-\alpha} q^{\beta_q} & \text{if } m_{\rm min} \leq m_2 \leq m_1 \leq m_{\rm max} \\ 0 & \text{otherwise} \end{cases}, \tag{2}$$

where $C(m_1)$ is chosen so that the marginal distribution is a power law in m_1: $p(m_1|m_{\rm min}, m_{\rm max}, \alpha, \beta_q) = m_1^{-\alpha}$.

Model A fixes $m_{\rm min} = 5 M_\odot$ and $\beta_q = 0$, whereas Model B fits for all four parameters. Equation 2 implies that the conditional mass ratio distribution is a power-law with $p(q \mid m_1) \propto q^{\beta_q}$. When $\beta_q = 0$, $C(m_1) \propto 1/(m_1 - m_{\rm min})$, as assumed in Abbott et al. (2016d, 2017e).

Model C (from Talbot & Thrane (2018)) further builds upon the mass distribution in Equation 2 by allowing for a second, Gaussian component at high mass, as well as introducing smoothing scales δm, which taper the hard edges of the low- and high-mass cutoffs of the primary and secondary mass power-law. The second Gaussian component is designed to capture a possible build-up of high-mass black holes created from pulsational pair instability supernovae. The tapered low-mass smoothing reflects the fact that parameters such as metallicity probably blur the edge of the lower mass gap, if it exists. Model C therefore introduces four additional model parameters, the mean, μ_m, and standard deviation, σ_m, of the Gaussian component, λ_m, the fraction of primary black holes in this Gaussian component, and δm the smoothing scale at the low mass end of the distribution.

The full form of this distribution is

$$\begin{aligned} p(m_1|\theta) &= \left[(1-\lambda_m) A(\theta) m_1^{-\alpha} \Theta(m_{\rm max} - m_1) + \lambda_m B(\theta) \exp\left(-\frac{(m_1 - \mu_m)^2}{2\sigma_m^2}\right)\right] S(m_1, m_{\rm min}, \delta m), \\ p(q|m_1, \theta) &= C(m_1, \theta) q^{\beta_q} S(m_2, m_{\rm min}, \delta m). \end{aligned} \tag{3}$$

The factors A, B, and C ensure each of the power-law component, Gaussian component, and mass ratio distributions are correctly normalized. S is a smoothing function which rises from zero at $m_{\rm min}$ to one at $m_{\rm min} + \delta m$ as defined in Talbot & Thrane (2018). Θ is the Heaviside step function.

2.4. *Parameterized Spin Models*

The black hole spin distribution is decomposed into independent models of spin magnitudes, a, and orientations, t. For simplicity and lacking compelling evidence to the contrary, we assume both black hole spin magnitudes in a binary, a_i, are drawn from a beta distribution (Wysocki et al. 2018):

$$p(a_i|\alpha_a, \beta_a) = \frac{a_i^{\alpha_a - 1}(1 - a_i)^{\beta_a - 1}}{\mathrm{B}(\alpha_a, \beta_a)}. \tag{4}$$

We can alternatively parameterize the beta distribution using the mean ($\mathbb{E}[a]$) and variance ($\mathrm{Var}[a]$) of the distribution, given by

$$\begin{aligned} \mathbb{E}[a] &= \frac{\alpha_a}{\alpha_a + \beta_a}; \\ \mathrm{Var}[a] &= \frac{\alpha_a \beta_a}{(\alpha_a + \beta_a)^2(\alpha_a + \beta_a + 1)}. \end{aligned} \tag{5}$$

We adopt a prior on the spin magnitude model parameters which are uniform over the values of $\mathbb{E}[a]$ and $\mathrm{Var}[a]$ which satisfy $\alpha_a, \beta_a \geq 1$, avoiding numerically-challenging singular spin distributions.

To describe the spin orientation, we assume that the tilt angles between each black hole spin and the orbital angular momentum, t_i, are drawn from a mixture of two distributions: an isotropic component, and a preferentially aligned component, represented by a truncated Gaussian distribution in $\cos t_i$ peaked at $\cos t_i = 1$ (Talbot & Thrane 2017)

$$\begin{aligned} p(\cos t_1, \cos t_2 | \sigma_1, \sigma_2, \zeta) = &\frac{(1-\zeta)}{4} \\ &+ \frac{2\zeta}{\pi} \prod_{i \in \{1,2\}} \frac{\exp\left(-(1 - \cos t_i)^2/(2\sigma_i^2)\right)}{\sigma_i \mathrm{erf}(\sqrt{2}/\sigma_i)}. \end{aligned} \tag{6}$$

The parameter ζ denotes the fraction of binaries which are preferentially aligned with the orbital angular momentum; $\zeta = 1$ implies all black hole spins are preferentially aligned and $\zeta = 0$ is an isotropic distribution of spin orientations. The typical degree of spin misalignment is represented by the σ_i. For spin orientations we explore two parameterized families of models:

- Gaussian (G): $\zeta = 1$.
- Mixture (M): $0 \leq \zeta \leq 1$.

The Gaussian model is motivated by formation in isolated binary evolution, with significant natal misalignment, while the mixture scenarios allow for an arbitrary combination of this scenario and randomly oriented spins, which arise naturally in dynamical formation.

2.5. *Redshift Evolution Models*

The previous two subsections described the probability distributions of intrinsic parameters $p(\xi)$ (i.e. masses and spins) that characterize the population of BBHs. In addition, we also measure the value of one extrinsic parameter of the population: the overall merger rate density $\mathcal{R}$. The models described in the previous two subsections assume that the distribution of intrinsic parameters is independent of cosmological redshift z, at least over the redshift range accessible to the LIGO and Virgo interferometers during the first two observing runs ($z \lesssim 1$). However, we consider an additional model in which the overall event rate evolves with redshift. We follow Fishbach et al. (2018) by parameterizing the evolving merger rate density $\mathcal{R}(z)$ in the comoving frame by

$$\mathcal{R}(z|\lambda) = \mathcal{R}_0 \left(1 + z\right)^{\lambda}, \tag{7}$$

where $\mathcal{R}_0$ is the rate density at $z = 0$. In this model, $\lambda = 0$ corresponds to a merger rate density that is uniform in comoving volume and source-frame time, while $\lambda \sim 3$ corresponds to a merger rate that approximately follows the star-formation rate in the redshift range relevant to the detections in O1 and O2 (Madau & Dickinson 2014). Various BBH formation channels predict different merger rate histories, ranging from rate densities that will peak in the future ($\lambda < 0$) to rate densities that peak earlier than the star-formation rate ($\lambda \gtrsim 3$). These depend on the formation rate history and the distribution of delay times between formation and redshift. In cases where we do not explicitly write the event rate density as $\mathcal{R}(z)$, it is assumed that the rate density $\mathcal{R}$ is constant in comoving volume and source-frame time.

2.6. *Statistical Framework*

The general model family, including the distributions of masses, spins and merger redshift, is therefore given by the distribution

$$\frac{\mathrm{d}N}{\mathrm{d}\xi \mathrm{d}z}(\theta) = \mathcal{R}\left(z\right) \left[\frac{\mathrm{d}V_c}{\mathrm{d}z}\left(z\right)\right] \frac{T_{\mathrm{obs}}}{1+z} p(\xi|\theta), \tag{8}$$

where N is the total number of mergers that occur within the detection horizon (i.e. the maximum redshift considered) over the total observing time, T_{obs}, as measured in the detector-frame, θ is the collection of all hyper-parameters that characterize the distribution, and dV_c/dz is the differential comoving volume per unit redshift. The merger rate density $\mathcal{R}(z)$ is related to N by

$$\mathcal{R}(z) = \frac{\mathrm{d}N}{\mathrm{d}V_c \mathrm{d}t}\left(z\right), \tag{9}$$

where t is the time in the source-frame, so that Eq. 8 can be written equivalently in terms of the merger rate density:

$$\frac{\mathrm{d}\mathcal{R}}{\mathrm{d}\xi}(z|\theta) = \mathcal{R}_0 p(\xi|\theta)(1+z)^{\lambda}. \tag{10}$$

We perform a hierarchical Bayesian analysis, accounting for measurement uncertainty and selection effects (Loredo 2004; Abbott et al. 2016d; Wysocki et al. 2018; Fishbach et al. 2018; Mandel et al. 2018). The likelihood of the observed GW data given the population hyperparameters θ that describe the general astrophysical distribution, $dN/d\xi dz$, is given by the inhomogeneous Poisson likelihood:

$$\mathcal{L}(\{d_n\}|\theta) \propto \\ e^{-\mu(\theta)} \prod_{n=1}^{N_{\rm obs}} \int \mathcal{L}(d_n|\xi, z) \frac{\mathrm{d}N}{\mathrm{d}\xi \mathrm{d}z}(\theta)\, \mathrm{d}\xi \mathrm{d}z, \tag{11}$$

where $\mu(\theta)$ is the expected number of detections as a function of the population hyper-parameters, $N_{\rm obs}$ is the number of detections, and $\mathcal{L}(d_n|\xi, z)$ is the individual-event likelihood for the nth detection having parameters ξ, z. In practice, we sample the likelihood $\mathcal{L}(d_n|\xi, z)$ using the parameter estimation pipeline LALInference (Veitch et al. 2015). Since LALInference gives us a set of posterior samples for each event, we first divide out the priors used in the individual-event analyses before applying Eq. 11 (Hogg et al. 2010; Mandel 2010). We note that the hyperparameter likelihood given by Eq. 11 reduces to the likelihood used in the O1 mass distribution analysis (Eq. D10 of Abbott et al. 2016d), which fit only for the shape, not the rate/ normalization of the mass distribution, if one marginalizes over the rate parameter with a flat-in-log prior $p(\mathcal{R}) \propto 1/\mathcal{R}$ (Fishbach et al. 2018; Mandel et al. 2018). For consistency with previous analyses, we adopt a flat-in-log prior on the rate parameter throghout this work.

The normalization factor of the posterior density in Bayes' theorem is the evidence — it is the probability of the data given the model. We are interested in the preferences of the data for one model versus another. This preference is encoded in the Bayes factor, or the ratio of evidences. The odds ratio is the Bayes factor multiplied by their ratio of the model prior probabilities. In all cases presented here, the prior model probabilities are assumed to be equal, and odds ratios are equivalent to Bayes factors.

In order to calculate the expected number of detections $\mu(\theta)$, we must understand the selection effects of our detectors. The sensitivity of GW detectors is a strong function of the binary masses and distance, and also varies with spin. For any binary, we define the sensitive spacetime volume $VT(\xi)$ of a network with a given sensitivity to be

$$VT(\xi) = T_{\rm obs} \int_0^{\infty} f(z|\xi) \frac{\mathrm{d}V_c}{\mathrm{d}z} \frac{1}{1+z} \mathrm{d}z, \tag{12}$$

where the sensitivity is assumed to be constant over the observing time, $T_{\rm obs}$, as measured in the detector-frame and $f(z|\xi)$ is the detection probability of a BBH with the given parameter set ξ at redshift z (O'Shaughnessy et al. 2010). The factor of $1/(1+z)$ arises from the difference in clocks timed between the source frame and the detector frame. For a given population with hyperparameters θ, we can calculate the total observed spacetime volume

$$\langle VT \rangle_\theta = \int_\xi p(\xi|\theta) VT(\xi) \mathrm{d}\xi, \tag{13}$$

where $p(\xi|\theta)$ describes the underlying distribution of the intrinsic parameters. We performed large scale simulation runs wherein the spacetime volume in the above equation is estimated by Monte-Carlo integration (Tiwari 2018). Allowing the merger rate to evolve with redshift, the expected number of detections is given by

$$\mu(\theta) = T_{\rm obs} \int_\xi \int_0^{\infty} p(\xi|\theta) f(z \mid \xi) \mathcal{R}(z) \frac{\mathrm{d}V_c}{\mathrm{d}z} \frac{1}{1+z} \mathrm{d}z \mathrm{d}\xi. \tag{14}$$

If the merger rate does not evolve with redshift, i.e., $\mathcal{R}(z) = \mathcal{R}_0$, this reduces to $\mu(\theta) = \mathcal{R}_0 \langle VT \rangle_\theta$.

Where not fixed, we adopt uniform priors on population parameters describing the models. Unless otherwise noted, for the event rate distribution we use a log-uniform distribution in $\mathcal{R}$, bounded between $[10^{-1}, 10^3]$. While this is a different form than the priors adopted in Abbott et al. (2018), we note that similar results are obtained on the rates (see Sec. 4), indicating that the choice of prior does not strongly influence the posterior distributions. We provide specific limits on all priors when the priors for a given model are introduced.

We often present the posterior population distribution (PPD) of various quantities. The PPD is the expected distribution of new mergers conditioned on previously obtained observations. It integrates the distribution of values (e.g., ξ, such as the masses and spins) conditioned on the model parameters (e.g, the power law index) over the posteriors obtained for the model parameters:

$$p(\xi_{\rm new}|\xi_{\rm observed}) = \int p(\xi_{\rm new}|\theta)p(\theta|\xi_{\rm observed})d\theta \quad (15)$$

It is a predictor for future merger values $\xi_{\rm new}$ given observed data $\xi_{\rm observed}$ and factors in the uncertainties imposed by the posterior on the model parameters. Note that the PPD does not incorporate the detector sensitivity, and therefore is not a straightforward predictor of the properties of future *observed* mergers.

3. THE MASS DISTRIBUTION

For context, Figure 4 in Abbott et al. (2018) illustrates the inferred masses for all of the significant BBH observations identified in our GW surveys in O1 and O2. Despite at least moderate sensitivity to total masses between 0.1 − 500 $M_\odot$, current observations occupy only a portion of the binary mass parameter space. Notably, we have not yet observed a pair of very massive (e.g., 100 $M_\odot$) black holes; a binary which is bounded away from equal mass in its posterior, or a binary with a component mass confidently below 5 $M_\odot$. In our survey, we also find a preponderance of observations at higher masses: six with significant posterior support above $30M_\odot$. In this section, we attempt to reconstruct the binary black hole merger rate as a function of the component masses using parameterized models. Table 2 summarizes the mass models adopted from Section 2.3 and the prior distributions for each of the parameters in those models.

3.1. *Parameterized Modeling Results*

Figure 1 shows our updated inference for the compact binary primary mass m_1 and mass ratio q distributions for several increasingly general population models. In addition to inferring the mass distribution, all of these calculations self-consistently marginalize over the parameterized spin distribution presented in Section 5 and the merger rate. Figures 2 and 3 show the posterior distribution on selected model hyperparameters.

If we assume the black hole masses are power-law distributed and fix the minimum black hole mass to be $m_{\rm min} = 5M_\odot$ (Model A), we find $\alpha = 0.4^{+1.3}_{-1.9}$, $m_{\rm max} = 41.6^{+9.0}_{-4.5}\,{\rm M}_\odot$. In Model B we infer the power-law index of the primary mass to be $\alpha = 1.6^{+1.5}_{-1.7}$ with corresponding limits $m_{\rm min} = 7.9^{+1.2}_{-2.5}\,{\rm M}_\odot$, $m_{\rm max} = 42.0^{+15.0}_{-5.7}\,{\rm M}_\odot$ (unless otherwise stated all credible intervals are symmetric 90% intervals).

Figure 3, shows the posterior over the population parameters present in A and B, as well as a second, Gaussian population parameterized with $m_{\rm max}$ and σ_m. λ_m is the mixing fraction of binaries in the Gaussian population versus the power law, with $\lambda_m = 0$ indicating only the power law component. The Gaussian component is centered at $\mu_m = 30.1^{+4.5}_{-6.9}\,{\rm M}_\odot$, has a width $\sigma_m = 5.5^{+3.8}_{-4.0}\,{\rm M}_\odot$, and is consistent with the parameters of the seven highest mass events in our sample as seen in Figure 4. Also as a consequence of this division, the inferred power-law is much steeper $\alpha = 7.3^{+4.2}_{-4.6}$ than Models A or B with and the posterior distribution returns the prior for $\alpha \gtrsim 4$. This in turn means that we cannot constrain the parameter $m_{\rm max}$ in Model C since the power-law component has negligible support above $\sim 45M_\odot$. In the intermediate regime, $\sim 15M_\odot - 25M_\odot$, Model C infers a smaller rate than Models A or B as a consequence of the steeper power-law behavior. The low mass smoothing allowed in this model also weakens constraints we can place on the minimum black hole mass, in this model we find $m_{\rm min} = 7.0^{+1.6}_{-1.7}\,{\rm M}_\odot$.

All models feature a parameter, $m_{\rm max}$, which defines a cutoff of the power law. However, the interpretation of that parameter within Model C is not a straightforward comparison with Models A and B, due to the presence of the Gaussian component at high mass and the large value of the power-law spectral index. Instead, to compare those two features, we compute the 99th percentile of the mass distribution inferred from the model PPDs (see Equation 15). Model A obtains 43.8 $M_\odot$, Model B obtains 42.8 $M_\odot$, and Model C obtains 41.8 $M_\odot$. Therefore, all models self-consistently infer a dearth of black holes above $\sim$ 45 $M_\odot$. This is determined by the lower limit for the mass of the most massive black hole in the sample because $m_{\rm max}$ can be *no smaller* than this value. Similarly, the models which allow $m_{\rm min}$ to vary (B and C) disfavor populations with $m_{\rm min}$ above $\simeq 9M_\odot$. This parameter is close to the largest allowed mass for the least massive black hole in the sample, for similar reasons.

The lower limits we place on $m_{\rm min}$ are dominated by our prior choices that constrain $m_{\rm min} \in [5, 10]\,M_\odot$ (see Table 2). For example, in Figure 2, the posterior on $m_{\rm min}$ becomes flat as $m_{\rm min}$ approaches the prior boundary at $5\,M_\odot$. Given current sensitivities, this is to be expected (Littenberg et al. 2015; Mandel et al. 2015). In the inspiral-dominated regime, the sensitive time-volume scales as $VT \sim m^{15/6}$ (Finn & Chernoff 1993); extending our inferred mass distributions and merger rates into the possible lower black hole mass gap from 3–5 $M_\odot$ (Özel et al. 2010; Farr et al. 2011b; Kreidberg et al. 2012) yields an expected number of detected BBH

Model	Mass Parameters								Spin Parameters			
	α	$m_{\max}$	$m_{\min}$	β_q	λ_m	μ_m	σ_m	δm	$\mathbb{E}[a]$	Var$[a]$	ζ	σ_i
A	[-4, 12]	[30, 100]	**5**	**0**	**0**	N/A	N/A	N/A	[0, 1]	[0, 0.25]	**1**	[0, 10]
B	[-4, 12]	[30, 100]	[5, 10]	[-4, 12]	**0**	N/A	N/A	N/A	[0, 1]	[0, 0.25]	**1**	[0, 10]
C	[-4, 12]	[30, 100]	[5, 10]	[-4, 12]	[0, 1]	[20, 50]	(0, 10]	[0, 10]	[0, 1]	[0, 0.25]	[0, 1]	[0, 4]

Table 2. Summary of models used in Sections 3, 4, and 5, with the prior ranges for the population parameters. The fixed parameters are in bold. Each of these distributions is uniform over the stated range. All models in this Section assume rates which are uniform in the comoving volume ($\lambda = 0$). The lower limit on $m_{\min}$ is chosen to be consistent with Abbott et al. (2018).

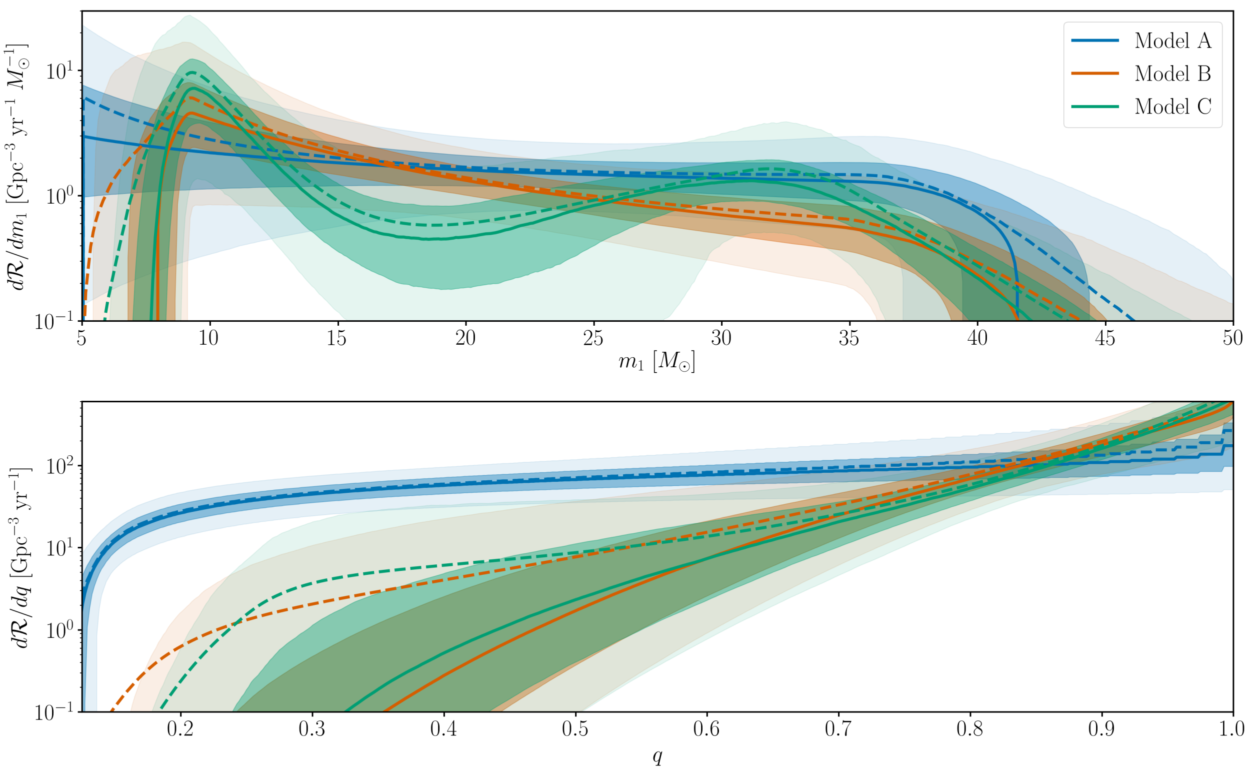

Figure 1. Inferred differential merger rate as a function of primary mass, m_1, and mass ratio, q, for three different assumptions. For each of the three increasingly complex assumptions A, B, C described in the text we show the PPD (dashed) and median (solid), plus 50% and 90% symmetric credible intervals (shaded regions), for the differential rate. The results shown marginalize over the spin distribution model. The falloff at small masses in models B and C is driven by our choice of the prior limits on the $m_{\min}$ parameter (see Table 2). All three models give consistent mass distributions within their 90% credible intervals over a broad range of masses, consistent with their near-unity evidence ratios (Table 3); in particular, the peaks and trough seen in Model C, while suggestive, are not identified at high credibility in the mass distribution.

mergers $\lesssim 1$. Thus, we are unable to place meaningful constraints on the presence or absence of a mass gap at low black hole mass.

Models B and C also allow the distribution of mass ratios to vary according to β_q. In these cases the inferred mass-ratio distribution favors comparable-mass binaries (i.e., distributions with most support near $q \simeq 1$), see panel two of Figure 1. Within the context of our parameterization, we find $\beta_q = 6.7^{+4.8}_{-5.9}$ for Model B and $\beta_q = 5.8^{+5.5}_{-5.8}$ for Model C. These values are consistent with each other and are bounded above zero at 95% confidence, thus implying that the mass ratio distribution is nearly flat or declining with more extreme mass ratios. The posterior on β_q returns the prior for $\beta_q \gtrsim 4$. Thus, we cannot say much about the relative likelihood of asymmetric binaries, beyond their overall rarity.

The distribution of the parameter controlling the fraction of the power law versus the Gaussian component in Model C is $\lambda_m = 0.4^{+0.3}_{-0.3}$, which peaks away from zero, implying that this model prefers a contribution to the

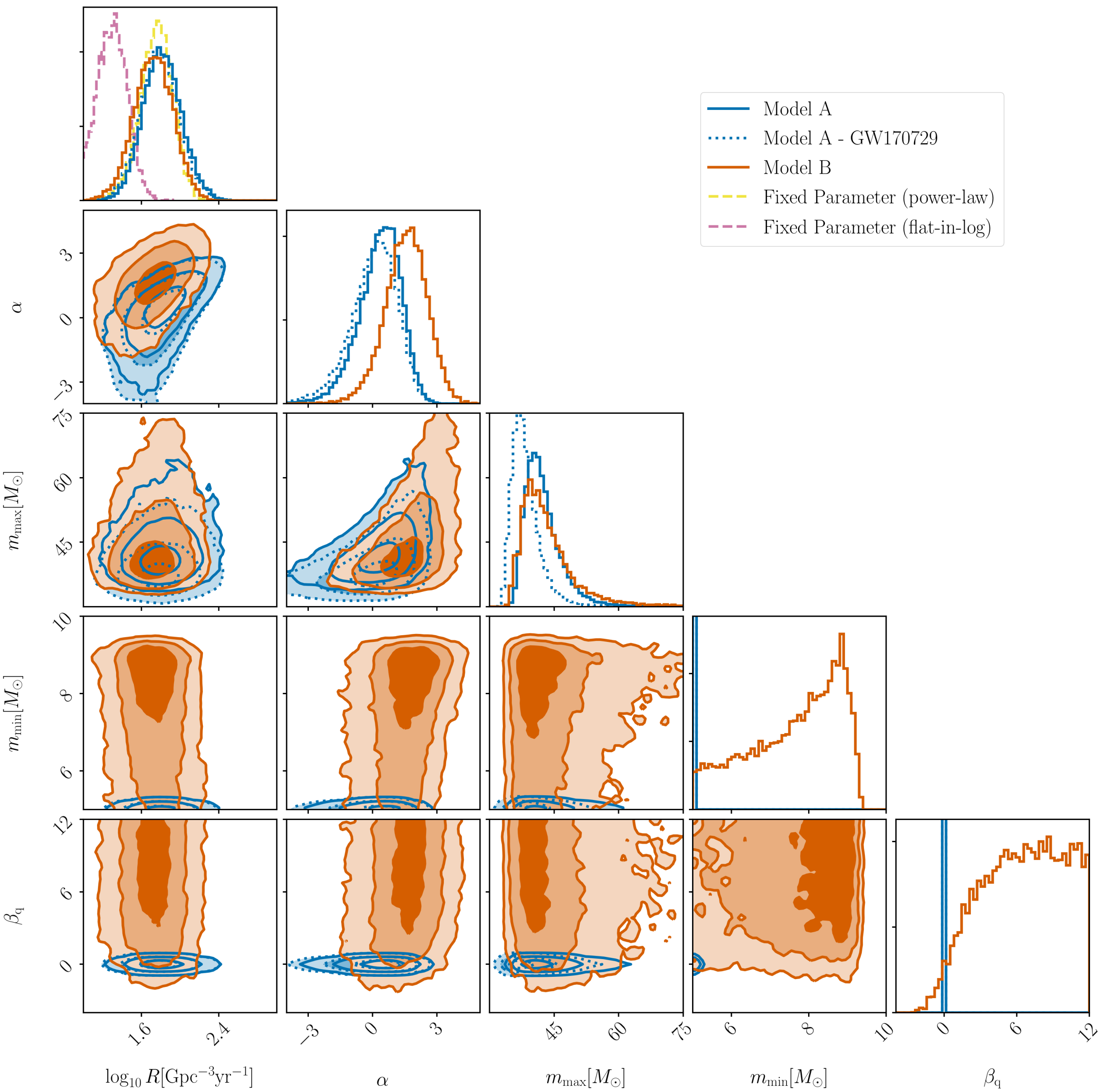

Figure 2. One- and two-dimensional posterior distributions for the hyperparameters describing Models A and B. Large values of α correspond to a mass distribution which rapidly decays with increasing mass. Large values of β correspond to a mass-ratio distribution which prefers equal mass binaries. Also shown is the one-dimensional posterior distribution for the merger rate discussed in Abbott et al. (2018), and the stability of Model A to the removal of the GW170729 event.

mass distribution from the Gaussian population in addition to the power laws modeled in A and B. To determine preference amongst the three models presented in this Section, we compute the Bayes factors comparing the mass models using a nested sampler (Skilling 2004), `CPNest` (Veitch et al. 2017). These are shown in Table 3. Model B, which allows $m_{\min}$ and β_q to vary is preferred over Model A ($\ln \mathrm{BF}^A_B = -0.97$). To isolate the contributions of the Gaussian component and low mass smoothing in Model C, we compute the Savage-Dickey density ratio, $p(\theta = 0)/p_{\rm prior}(\theta = 0)$, equivalent to the Bayes factor comparing without and with the feature. The model including a Gaussian component in addition to the power-law distribution is preferred over the pure power-law models ($\ln \mathrm{BF}^{\lambda=0}_C = -2.12$); nevertheless, all models infer mass distributions that agree within their 90% credible bounds (see Figure 1). We are unable to distinguish between a gradual or sharp cutoff at low

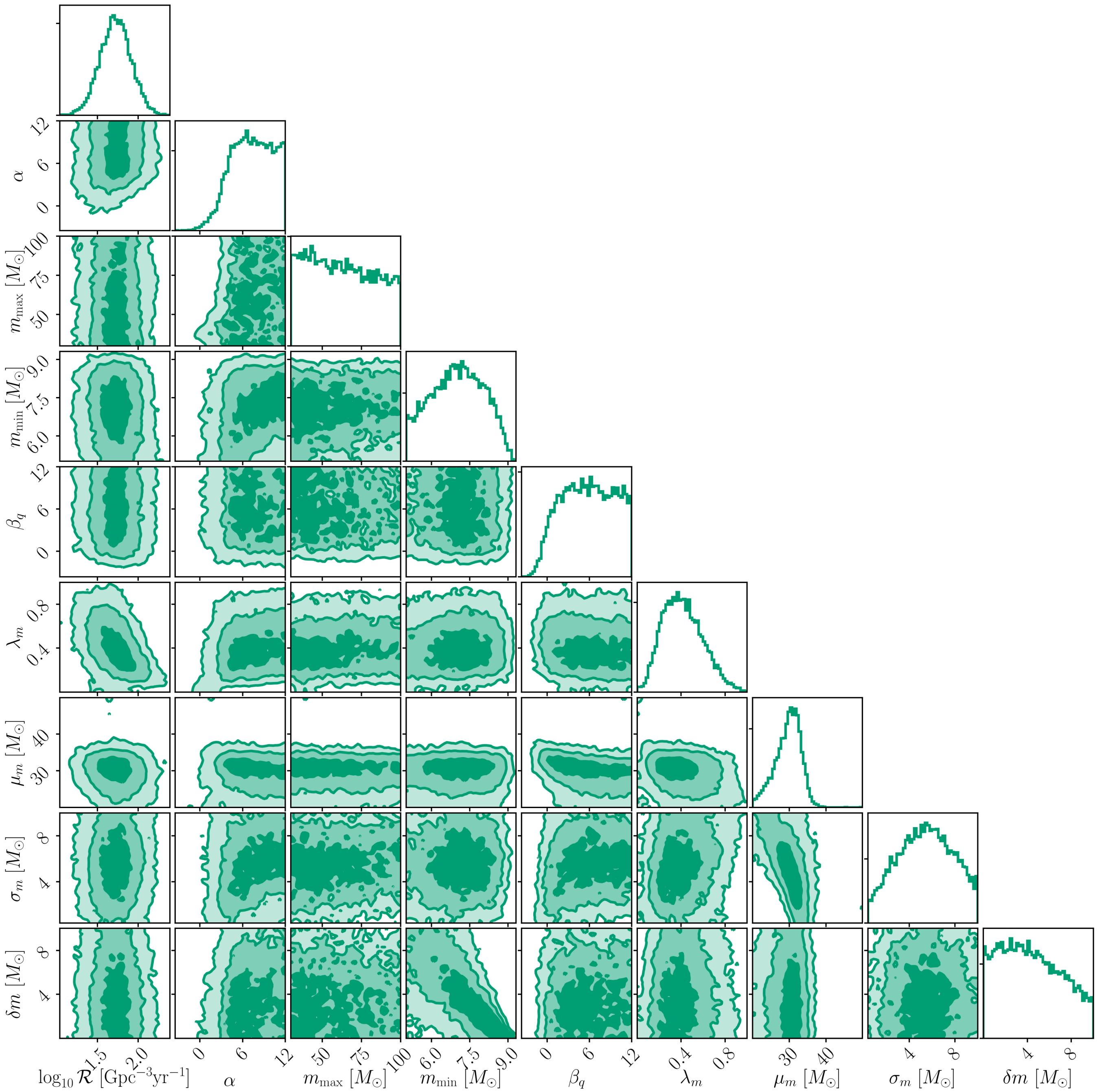

Figure 3. One- and two-dimensional posterior distributions for the hyperparameters describing Model C. This model consists of the power-law distribution in Model B with an additional Gaussian component at high mass. The parameters α, β, $m_{\rm max}$, and $m_{\rm min}$ describe the power-law component. The Gaussian has mean μ_m and standard deviation σ_m. The fraction of black holes in the Gaussian component is λ_m. This model also allows for a gradual turn-on at low masses over a mass range δ_m.

Model	A	B	C, $\lambda_m = 0$	C, $\delta_m = 0$
$\ln \mathrm{BF}^i_C$	-2.37	-1.40	-2.12	0.14

Table 3. The log Bayes factor comparing each of the models described in Table 2 to the most complex model, Model C. The evidence for the three mass models is computed using nested sampling, while the limits $\lambda_m = 0$ and $\delta_m = 0$ of Model C are computed using the Savage-Dickey density ratio.

mass ($\ln \mathrm{BF}_C^{\delta_m=0} = 0.14$). This is unsurprising, since we are less sensitive to structure in the mass distribution at low masses (Talbot & Thrane 2018).

All three models produce consistent results for the marginal merger rate distribution, as discussed in Section 4.

The analysis above includes all ten binary black hole detections, though not all events have the same statistical detection confidence (Gaebel et al. 2018). To assess the stability of our results against systematics in the estimated significance, we have repeated these analyses after omitting the least significant detection. For our sample, the least significant detection, GW170729, is also the most massive binary. Most features we derive from our observations remain unchanged, with one exception shown in Figure 2: since we have omitted the most massive binary, the maximum black hole mass $m_{\max}$ reported in models A and B is decreased by about 5 $M_{\odot}$. Without GW170729, the $m_{\max}$ distribution is $37.8^{+7.1}_{-3.5}\,\mathrm{M}_{\odot}$ for Model A and $36.9^{+14.8}_{-4.1}\,\mathrm{M}_{\odot}$ for Model B. This is consistent with the difference between GW170729 and the next highest mass binary, GW170823, when comparing the less massive end of their primary mass posteriors.

3.2. *Comparison with Theoretical and Observational Models*

Previous modeling of the primary mass distribution with a power law distribution (Abbott et al. 2016d) was last updated with the discovery of GW170104 (Abbott et al. 2017e). This analysis measured spectral index of the the power law to be $\alpha = 2.3^{+1.3}_{-1.4}$ at 90% confidence assuming a minimum black hole mass of 5 $M_{\odot}$ and maximum total mass of 100 $M_{\odot}$. None of our models directly emulate this one, but Model A is the closest analog. When allowing $m_{\max}$ to vary, 100 $M_{\odot}$ is strongly disfavored, and as a consequence of the lower $m_{\max}$, the power law index inferred is also much shallower than previously obtained (Fishbach & Holz 2017).

In Figure 4, we highlight the two mass gaps predicted by models of stellar evolution: the first gap between ~ 2 and ~ 5 $\mathrm{M}_{\odot}$ and the second between ~ 50 $\mathrm{M}_{\odot}$ and ~ 150 $\mathrm{M}_{\odot}$, compared against the observed black holes. A set of tracks (Spera & Mapelli 2017) relating the progenitor mass and compact object is also shown for reference purposes. The tracks are subject to many uncertainties in stellar and binary evolution, and only serve as representative examples. We discuss some of those uncertainties in the context of our results below.

The minimum mass of a black hole and the existence of a mass gap between neutron stars and black holes (lower gray shaded area, right panel of Figure 4) are currently debated. Claims (Özel et al. 2010; Farr et al. 2011b) of the existence of a mass gap between the heaviest neutron stars (~ 2 $\mathrm{M}_{\odot}$) and the lightest black holes (~ 5 $\mathrm{M}_{\odot}$) are based on the sample of about a dozen X-ray binaries with dynamical mass measurements. However, Kreidberg et al. (2012) suggested that the dearth of observed black hole masses in the gap could be due to a systematic offset in mass measurements. We can see in Figure 4 that none of the observed binaries sit in this gap, but the sample is not sufficient to definitively confirm or refute the existence of this mass gap.

From the first six announced BBH detections, Fishbach & Holz (2017) argued that there is evidence for missing black holes with mass greater than $\gtrsim 40$ $\mathrm{M}_{\odot}$. The existence of this second mass gap — see the upper grey shaded area in the right panel of Figure 4 between ~ 50 $\mathrm{M}_{\odot}$ and ~ 150 $\mathrm{M}_{\odot}$ — has been further explored by Talbot & Thrane (2018); Wysocki et al. (2018); Roulet & Zaldarriaga (2018); Bai et al. (2018). This gap might arise from the combined effect of pulsational pair instability (Barkat et al. 1967; Heger et al. 2003; Woosley et al. 2007; Woosley 2017) and pair instability (Fowler & Hoyle 1964; Ober et al. 1983; Bond et al. 1984) supernovae. Predictions for the maximum mass of black holes born after pulsational pair-instability supernovae are $\sim 50 M_{\odot}$ (Belczynski et al. 2016b; Spera & Mapelli 2017). Our inferred maximum mass is consistent with these predictions.

4. MERGER RATES AND EVOLUTION WITH REDSHIFT

As illustrated in previous work (Abbott et al. 2016e; Abbott et al. 2018; Fishbach & Holz 2017; Wysocki et al. 2018; Fishbach et al. 2018), the inferred binary black hole merger rate depends on and correlates with our assumptions about their intrinsic mass (and to a lesser extent, spin) distribution. In the most recent catalog of GW BBH events (Abbott et al. 2018), we infer the overall BBH merger rate for two fixed populations. The first of these populations follows the power-law model given by Equation 2 with $\alpha = 2.3$, $\beta_q = 0$, $m_{\min} = 5 M_{\odot}$, and $m_{\max} = 50 M_{\odot}$. The second population follows a distribution in which both black hole masses are inde-

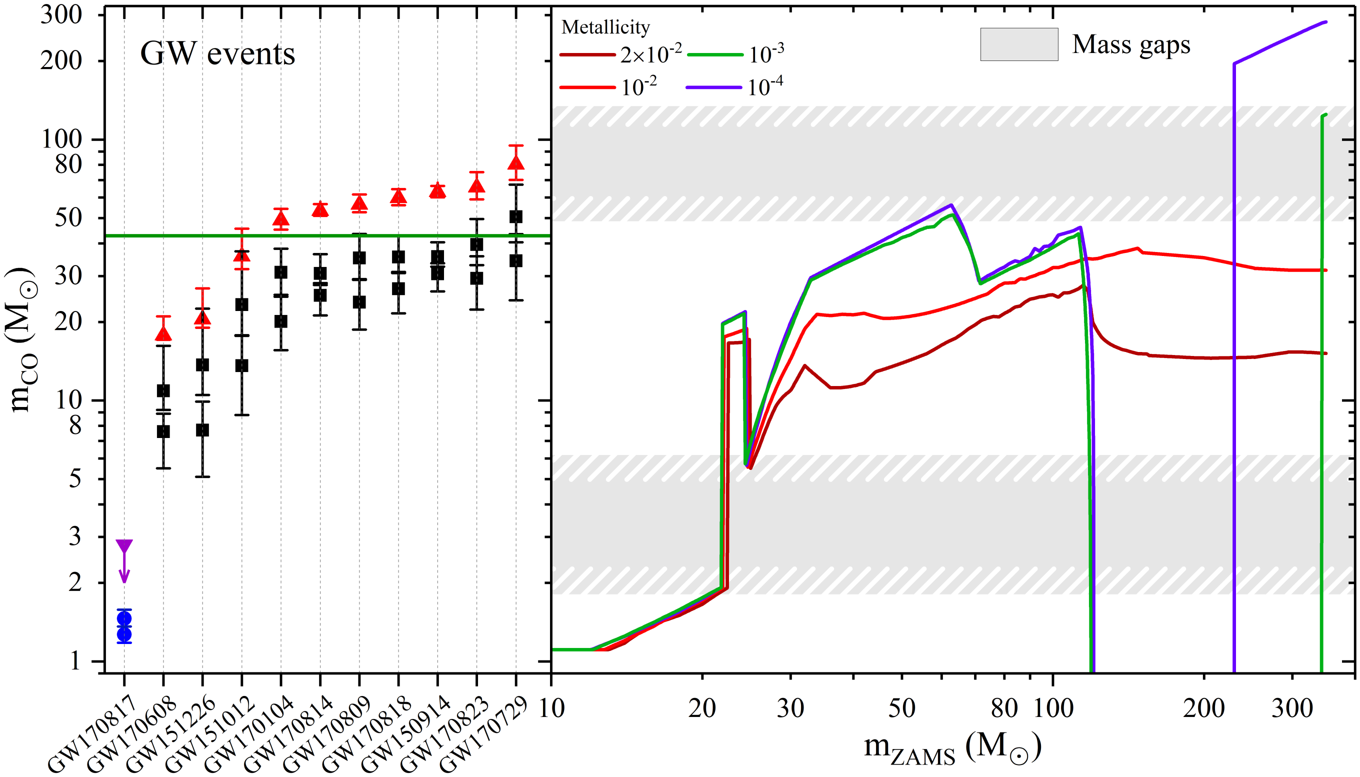

Figure 4. The left-hand panel shows compact object masses ($m_{\rm CO}$) from GW detections in O1 and O2, with the black squares and error bars representing the component masses of the merging black holes and their uncertainties, and red triangles representing the mass and associated uncertainties of the merger products. The horizontal green line shows the 99th percentile of the mass distribution inferred from the PPD (cfr. Section 3.1). In the right-hand panel, the predicted compact-object mass is shown as a function of the zero-age main sequence mass of the progenitor star ($m_{\rm ZAMS}$) and for four different metallicities of the progenitor star (ranging from $Z = 10^{-4}$ to $Z = 2 \times 10^{-2}$, Spera & Mapelli 2017). This model accounts for single stellar evolution from the PARSEC stellar-evolution code (Bressan et al. 2012), for core-collapse supernovae (Fryer et al. 2012), and for pulsational-pair instability and pair-instability supernovae (Woosley 2017). The shaded areas represent the lower and upper mass gaps. There is uncertainty as to the final product of GW170817. It is shown in the left-hand panel to emphasize that BNS mergers might fill the lower gap.

pendently drawn from a flat-in-log distribution:

$$p(m_1, m_2) \propto \frac{1}{m_1 m_2}, \tag{16}$$

subject to the same mass cutoffs $5M_\odot < m_2 < m_1 < 50M_\odot$ as the fixed power-law population. Both the power-law and flat-in-log populations assume an isotropic and uniform-magnitude spin distribution ($\alpha_a = \beta_a = 1$). These two fixed-parameter populations are used to estimate the population-averaged sensitive volume $\langle VT \rangle$ with a Monte-Carlo injection campaign as described in Abbott et al. (2018), with each population corresponding to a different $\langle VT \rangle$ because of the strong correlation between the mass spectrum and the sensitive volume. Under the assumption of a constant-in-redshift rate density, these $\langle VT \rangle$ estimates yield two different estimates of the rate: 57^{+40}_{-25} Gpc^{-3} yr^{-1}for the $\alpha = 2.3$ population, and $19^{+13}_{-8.2}$ Gpc^{-3} yr^{-1}for the flat-in-log population.

While the two fixed-parameter distributions are structurally consistent with prior work, they do not incorporate all information about the mass, mass ratio, spin distribution, and redshift evolution suggested by our observations in O1 and O2. In this section, rather than fixing the mass and spin distribution, we estimate the rate by marginalizing over the uncertainty in the underlying population, which we parameterize with the mass and spin models employed in Sections 3 and 5. When carrying out these analyses, it is computationally infeasible to determine $VT(\xi)$ for each point in parameter space with the full Monte-Carlo injection campaign described in Abbott et al. (2018), so we employ the semi-analytic methods described in Appendix A. Furthermore, while the rate calculations in Abbott et al. (2018) incorporate all triggers down to a very low threshold and fit the number of detections by modeling the signal and background distributions in the detection pipelines (Farr et al. 2015; Abbott et al. 2016e), in this work we fix a high detection threshold, which sets the number of detections to $N_{\rm obs} = 10$. In principle, our results are sensitive to the choice of threshold, but this effect is likely to be much smaller than the statistical uncertainties (Gaebel et al. 2018). The choice of detection threshold is further discussed in Appendix A. The full set of models used in this section are enumerated in Table 4.

In these calculations, we first maintain the assumption in Abbott et al. (2018) that the merger rate is uniform in comoving volume and source-frame time, as discussed in Section 2. We then relax this assumption and consider a merger rate that evolves in redshift according to Equation 7, fitting the mass distribution jointly with the rate density as a function of redshift.

4.1. *Non-Evolving Merger Rate*

We first consider the case of a uniform in volume merger rate, and examine the effects of fitting the rate jointly with the distribution of masses and spins. The first column in Figures 2 and 3 shows the results of self-consistently determining the rate using the models for the mass and spin distribution described in the previous two sections. For Models B and C we deduce a merger rate between $\mathcal{R}_0 = 25.9 - 108.5\,\mathrm{Gpc}^{-3}\,\mathrm{yr}^{-1}$. Adopting Model A for the mass distribution yields a slightly higher rate estimate, $\mathcal{R}_0 = 31.4 - 140.4\,\mathrm{Gpc}^{-3}\,\mathrm{yr}^{-1}$, as this model fixes $m_{\rm min} = 5M_\odot$, whereas Models B and C favor a higher minimum mass and therefore larger population-averaged sensitive volumes. The rate estimates are consistent between all mass models considered, including the results presented for the fixed-parameter power-law model in Abbott et al. (2018). However, the fixed-parameter models in Abbott et al. (2018) are disfavored by our full fit to the mass distribution, particularly with respect to the maximum mass. Our results favor maximum masses $\lesssim 45M_\odot$, rather than $50M_\odot$ as used in Abbott et al. (2018), and power-law slopes closer to $\alpha \sim 1$. For this reason, although we infer a mass distribution slope that is similar to the flat-in-log population from Abbott et al. (2018), we infer a rate that is closer to the rate inferred for the fixed-parameter power-law model[2]. While $\langle VT \rangle$ gets larger (implying a smaller rate estimate) as α is decreased, decreasing $m_{\rm max}$ has the opposite effect, and so the $\langle VT \rangle$ for the fixed-parameter power-law model is similar to the $\langle VT \rangle$s for our best-fit mass distributions, which favor smaller α and smaller $m_{\rm max}$.

[2] The flat-in-log population (Equation 16) cannot be parameterized by the mass models A, B and C used in this work, because the mass ratio distribution takes a different form. However, it is very close to Model A with $\alpha = 1$.

We note that while our analysis differs from the rate calculations in Abbott et al. (2018) by the choice of prior on the rate parameter (log-uniform in this work compared to a Jeffreys prior $p(\mathcal{R}) \propto \mathcal{R}^{-0.5}$ in Abbott et al. (2018)), adopting a Jefferys prior has a negligible effect on our rate posteriors. For example, under a log-uniform prior, we recover a rate for Model A of $63.7^{+74.6}_{-33.4}\,\mathrm{Gpc}^{-3}\,\mathrm{yr}^{-1}$, whereas under a Jeffreys prior this shifts by only $\sim 10\%$ to $57.4^{+65.9}_{-30.2}\,\mathrm{Gpc}^{-3}\,\mathrm{yr}^{-1}$.

4.2. *Evolution of the Merger Rate with Redshift*

As discussed in the introduction, most formation channels predict some evolution of the merger rate with redshift, due to factors including the star-formation rate, time-delay distribution, metallicity evolution, and globular cluster formation rate (Dominik et al. 2013; Belczynski et al. 2016a; Mandel & de Mink 2016; Rodriguez & Loeb 2018). Therefore, in this section, we allow the merger rate to evolve with redshift, and infer the redshift evolution jointly with the mass distribution. For simplicity, we adopt the two-parameter Model A for the mass distribution and fix spins to zero for this analysis. As discussed in Section 3, the additional mass and spin degrees of freedom have only a weak effect on the inferred merger rate. We assume the redshift evolution model given by Equation 7. Because massive binaries are detectable at higher redshifts, the observed redshift evolution correlates with the observed mass distribution of the population, and so we must fit them simultaneously. However, as in Fishbach et al. (2018), we assume that the underlying mass distribution does not vary with redshift. We therefore fit the joint mass-redshift distribution according to the model:

$$\frac{d\mathcal{R}}{dm_1 dm_2}(z) = \mathcal{R}_0 p(m_1, m_2 \mid \alpha, m_{\rm max})(1+z)^\lambda \tag{17}$$

Figure 5 shows the merger rate density as a function of redshift (blue band), compared to the rate inferred in Abbott et al. (2018) for the two fixed-parameter models (green and red). The joint posterior PDF on λ, α, and $m_{\rm max}$, marginalized over the local rate parameter $\mathcal{R}_0$, is shown in Figure 6. Compared to the constraints on α and $m_{\rm max}$ discussed in Section 3, which assume a constant-in-redshift merger rate density, allowing for additional freedom in the redshift distribution of BBHs relaxes the constraints on the mass distribution parameters, especially the power-law slope α. Under the assumption of a constant merger rate density, Model A in Section 3 finds $\alpha = 0.4^{+1.3}_{-1.9}$, $m_{\rm max} = 41.6^{+9.0}_{-4.5}\,\mathrm{M}_\odot$, whereas allowing for redshift evolution yields $\alpha = 1.6^{+1.6}_{-2.0}$, $m_{\rm max} = 42^{+12}_{-5}\ M_\odot$ when analyzing the sample of 10 BBHs from O1 and O2. There is

Model	Mass Model	Rate Parameters λ	Spin Parameters α_a	β_a	$\mathbb{E}[a]$	Var$[a]$
Fixed Parameter (power-law)	A, with $\alpha = 2.3$, $m_{\max} = 50 M_\odot$	**0**	**1**	**1**	N/A	N/A
Fixed Parameter (flat-in-log)	Equation 16	**0**	**1**	**1**	N/A	N/A
Non-Evolving	A, B, C	**0**	N/A	N/A	[0,1]	[0, 0.25]
Evolving[a]	A	[-25, 25]	N/A	N/A	**0**	**0**

[a]This model assumes the black holes have zero spin.

Table 4. Summary of models in Section 4, with prior ranges for the population parameters determining the rate models. The fixed parameter models are drawn from Abbott et al. (2018). The fixed parameters are in bold. Each of these distributions is uniform over the stated range; as previously, we require $\alpha_a, \beta_a \geq 1$. Details of the mass models listed here are described in Table 2.

a strong correlation between the mass power-law slope and the redshift evolution parameter, although the maximum mass parameter remains well-constrained. As in Section 3, we carry out a leave-one-out analysis, excluding the most massive and distant BBH, GW170729 from the sample (red curves in Figure 6). Without GW170729, the marginalized mass-distribution posteriors become $\alpha = 0.8^{+1.7}_{-2.2}$, $m_{\max} = 38^{+10}_{-4}$ $M_\odot$.

Marginalizing over the two mass distribution parameters and the redshift-evolution parameter, the merger rate density is consistent with being constant in redshift ($\lambda = 0$), and in particular, it is consistent with the rate estimates for the two fixed-parameter models in Abbott et al. (2018), as shown in Figure 5. However, we find a preference for a merger rate density that increases at higher redshift ($\lambda \geq 0$) at 0.88 credibility. This preference becomes less significant when GW170729 is excluded from the analysis, because this event likely merged at redshift $z \gtrsim 0.5$, close to the O1-O2 detection horizon. Although GW170729 shifts the posterior towards larger values of λ, implying a stronger redshift evolution of the merger rate, the posterior remains well within the uncertainties inferred from the remaining nine BBHs. When including GW170729 in the analysis, we find $\lambda = 6.5^{+9.1}_{-9.3}$ at 90% credibility, compared to $\lambda = 0.9^{+9.8}_{-10.8}$ when excluding GW170729 from the analysis. With only 10 BBH detections so far, the wide range of possible values for λ is consistent with most astrophysical formation channels. The precision of this measurement will improve as we accumulate more detections in future observing runs and may enable us to discriminate between different formation rate histories or time-delay distributions (Sathyaprakash et al. 2012; Van Den Broeck 2014; Fishbach et al. 2018).

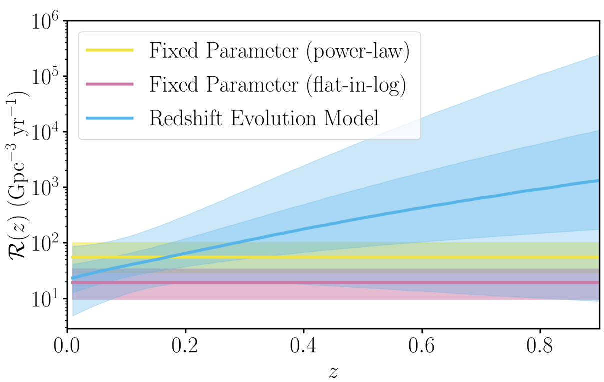

Figure 5. Constraints on evolution of the BBH merger rate density as a function of redshift. Including the 10 BBHs from O1 and O2 in our analysis, we find a preference for a merger rate that increases with increasing redshift. The solid blue line gives the posterior median merger rate density and dark and light bands give 50% and 90% credible intervals. In green and red, the solid line and shaded region shows the median and 90% credible interval of the rate inferred for each of the fixed-parameter models.

5. THE SPIN DISTRIBUTION

The GW signal depends on spins in a complicated way, but at leading order, and in the regime we are interested in here, some combinations of parameters have more impact on our inferences than others, and thus are measurable. One such parameter is $\chi_{\rm eff}$. For binaries which are near equal mass, we can see from Equation 1 that only when black hole spins are high and aligned with the orbital angular momentum $\chi_{\rm eff}$ will be measurably greater than zero. Figure 5 in Abbott et al. (2018) illustrates the inferred $\chi_{\rm eff}$ spin distributions for all of the BBHs identified in our GW surveys in O1 and O2. With a few exceptions, current observations of BBH spin are not consistent with large, aligned black hole spins. Only GW170729 and GW151226 show significant evidence for positive $\chi_{\rm eff}$; the rest of the posteriors cluster around $\chi_{\rm eff} = 0$.

Despite these degeneracies, several tests have been proposed to use spins to constrain BBH formation channels (Vitale et al. 2017; Farr et al. 2017, 2018; Stevenson et al. 2017a; Talbot & Thrane 2017; Wysocki et al.

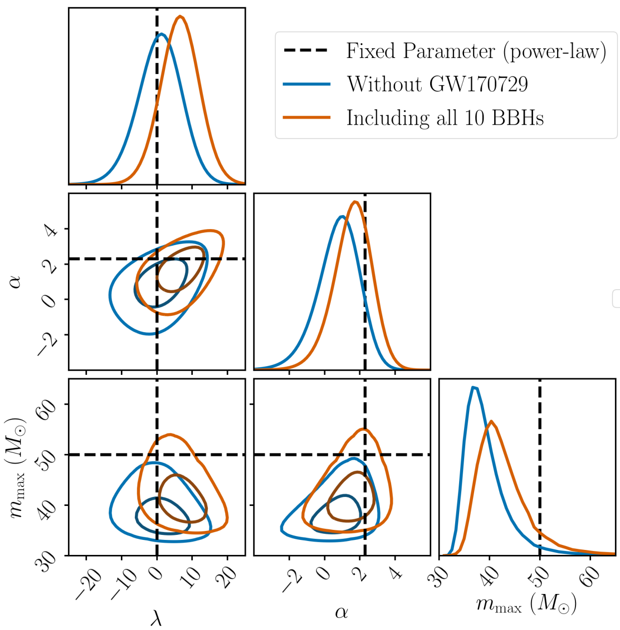

Figure 6. The posterior PDF on the redshift evolution parameter λ, mass power-law slope α, and maximum mass $m_{\max}$, marginalized over the local rate parameter $\mathcal{R}_0$, and assuming a flat prior on λ, α, and $m_{\max}$ and a flat-in-log prior on $\mathcal{R}_0$. In order to analyze the stability of the model against outliers, we repeat the analysis once with the sample of 10 BBHs (results shown in blue), and once excluding the most distant and massive event in our sample, GW170729 (results shown in red). The contours show 50% and 90% credible intervals. The dashed black lines show the values of hyper-parameters assumed for the fixed-parameter power-law model. We infer a redshift evolution that is consistent with a flat in comoving volume and source-frame time merger rate ($\lambda = 0$) with a preference for $\lambda \geq 0$ at 0.88 credibility when considering all 10 events. This preference becomes less significant with the exclusion of GW170729 from the analysis. The inferred power-law slope and maximum mass is consistent with the values inferred in Section 3. This analysis recovers a broader posterior on the mass power-law slope because of the correlation with the redshift evolution parameter, but the maximum mass remains well-constrained at $\lesssim 45 M_\odot$.

2018). Drawing upon these methods, we now seek to estimate the black hole spin magnitude and misalignment distributions, under different assumptions regarding isotropy or alignment.

5.1. *Spin Magnitude and Tilt Distributions*

We examine here the individual spin magnitudes and tilt distributions. Throughout this section, when referring to the parametric models, we also allow the merger rate and population parameters describing the most general mass model to vary (e.g., Model C, see Table 2). Changing the parameterization of the mass model does not significantly change our inferences about the spin distribution. However, to account for degeneracies between mass and spin that grow increasingly significant for longer, low-mass signals (Baird et al. 2013), we must consistently model the mass and spin distributions together. The prior distribution on the Beta moments are all identical across all mass models tested; see Table 5 for a summary of the models and priors used in this Section.

The inferred distributions of spin magnitude are shown in Figure 7. The top panel shows the PPD as well as the median and associated uncertainties on the spin magnitude inferred from the parametric Mixture model. It marginalizes over all other parameters, including the mass parameters in Model C, and the spin mixture fraction. We observe that spin distributions which decline with increasing magnitude are preferred; in terms of our Beta function parameterization, these have mean spin $\mathbb{E}[a] < 1/2$ or equivalently have $\beta_a > \alpha_a$, at posterior probability 0.79. We find that 90% of black hole spins in BBHs are less than $a \leq 0.55$ from the PPD, and 50% of black hole spins are less than $a \leq 0.27$. We find similar conclusions if both black hole spins are drawn from different distributions (i.e., 90% of black hole spins on the more massive black hole are less than 0.7). The observed distribution also necessarily has a peak, introduced in part by our choice of prior to avoid singularities in the Beta distributions (i.e., $p(a = 0) = p(a = 1) = 0$ for almost all spin distributions). Based on extended analysis including a wider range of α_a and on the model selection calculations described in Appendix B, we believe the data could support spin distributions more concentrated towards zero spin. The recovered spin distribution is driven by disfavoring large spins, which are difficult to reconcile with the observed population.

We also compute the posterior distribution for the magnitude of black hole spins from $\chi_{\rm eff}$ measurements by modeling the distribution of black hole spin magnitudes non-parametrically with five bins, assuming either an isotropic or aligned population following Farr et al. (2018). We show in the bottom panel of Figure 7 that under the aligned scenario there is preference for small black hole spin, inferring 90% of black holes to have spin magnitudes below $0.6^{+0.24}_{-0.28}$. However, when spins are assumed to be isotropic the distribution is relatively flat, with 90% of black hole spin magnitudes below $0.8^{+0.15}_{-0.24}$. Thus, the non-parametric analysis produces conclusions consistent with our parametric analyses described above. These conclusions are also reinforced by computing the Bayes factor for a set of fixed parameter models of spin magnitude and orientation in Appendix B. There we find that the very low

Model	Mass Model	Spin Parameters				
		$\mathbb{E}[a]$	Var$[a]$	α_a, β_a	ζ	σ_i
Gaussian (G)	C	[0, 1]	[0, 0.25]	≥ 1	**1**	[0, 4]
Mixture (M)	C	[0, 1]	[0, 0.25]	≥ 1	[0, 1]	[0, 4]

Table 5. Summary of spin distribution models examined in Section 5.1, with prior ranges for the population parameters determining the spin models. The fixed parameters are in bold. Each of these distributions is uniform over the stated range, with boundary conditions such that the inferred parameters α_a, β_a must be ≥ 1. Details of the mass model listed here is described in Table 2.

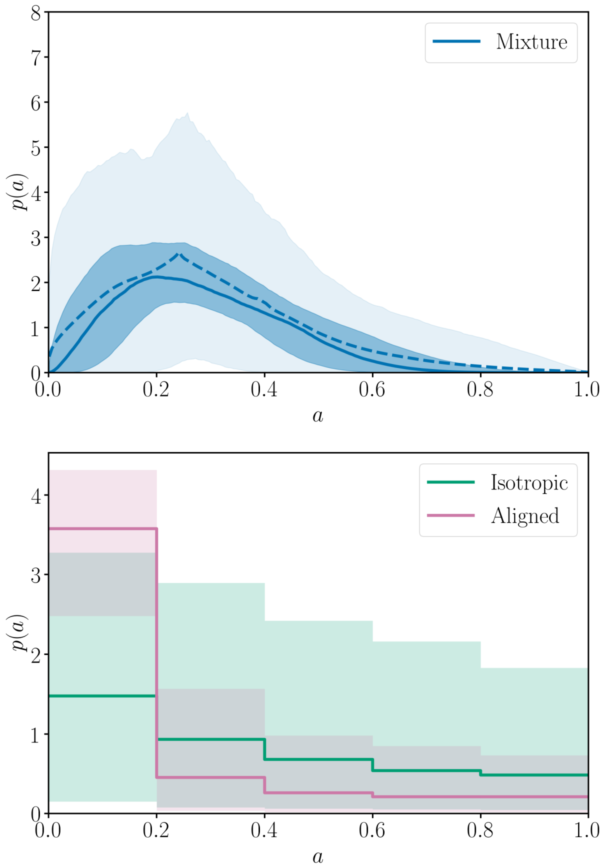

Figure 7. Inferred distribution of spin magnitude for a parametric (top) and non-parametric binned model (bottom). The solid lines show the median and the dashed line shows the PPD. The shaded regions denote the 50% and 90% symmetric intervals. In the bottom panel, the distribution of spin magnitude is inferred over five bins, assuming either aligned (green) or isotropic (blue) population. The solid lines denote the median, and the shaded regions denote the central 90% posterior credible bounds. In both cases, the magnitude is consistent within the uncertainties with the parametric results.

spin magnitude model is preferred in all three orientation configurations tested (see Figure 11 and Table 6 for details).

Figure 8 shows the inferred distribution of the primary spin tilt for the more massive black hole. In the Gaussian model ($\zeta = 1$), all black hole spin orientations are drawn from spin tilt distributions which are preferentially aligned and parameterized with σ_i. In that model, the σ_i distributions do not differ appreciably from the their flat priors. As such, the inferred spin tilt distribution are influenced by large σ_i and the result resembles an isotropic distribution. The Mixture distribution does not return a decisive measurement of the mixture fraction, obtaining $\zeta = 0.5^{+0.4}_{-0.5}$. Since the Gaussian model is a subset of the Mixture model, we can compare preferences via the Savage-Dickey ratio. The log Bayes factor for $\zeta = 1$ is $\ln \mathrm{BF} = 0.09$, indicating virtually no preference for any particular orientation distribution. While we allow both black holes to have different typical misalignment, the inference on the second tilt is less informative than the primary. The inferred distribution for $\cos t_2$ is similar to $\cos t_1$, but also closer to the prior.

The mixture fraction distribution is also modelled with the fixed parameter models in Appendix B. The fixed magnitude distributions considerd in Appendix B prefer isotropic to aligned, but the preference is weakened for distributions concentrated at lower spins. A few exceptions occur for the very low spin fixed mass ratio models, with aligned models being slightly preferred.

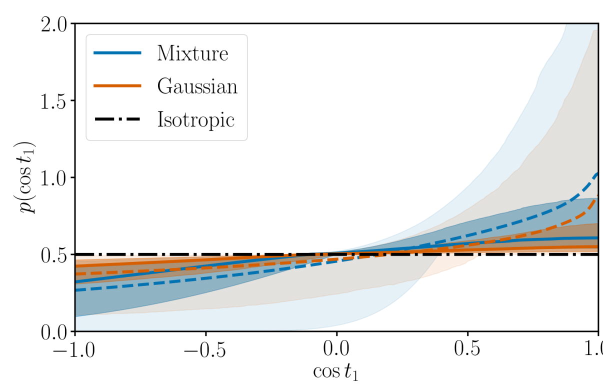

Figure 8. Inferred distribution of cosine spin tilt for the more massive black hole for two choices of prior (see Section 2.4). The dash-dotted line denotes a completely isotropic distribution (see Appendix B). The solid lines show the median. The shaded regions denote the 50% and 90% symmetric intervals and the dashed line denotes the PPD.

In general, we are not able to place strong constraints on the distribution of spin orientations. We elaborate in Appendix B.4 on how our black hole spin measurements are not yet informative enough to discern between isotropic and aligned orientation distribution via $\chi_{\rm eff}$.

5.2. *Interpretation of Spin Distributions*

The spins of black holes are affected by a number of uncertain processes which occur during the evolution of the binary. As a consequence, the magnitude distribution is difficult to predict from theoretical models of these processes alone. While the spin of a black hole should be related to the rotation of the core of its progenitor star, the amount of spin which is lost during the final stages of the progenitor's life is still highly uncertain. The core rotational angular momentum before the supernova can be changed from the birth spin of the progenitor by several processes (Langer 2012; de Mink et al. 2013). Examples include mass transfer (Shu & Lubow 1981; Packet 1981), or tidal interactions (Petrovic et al. 2005), as well as internal mixing of the stellar layers across the core-envelope boundary via magnetic torquing (Spruit 2002; Maeder & Meynet 2003) and gravity waves (Talon & Charbonnel 2005, 2008; Fuller et al. 2015). In principle, an off-center supernova explosion could also impart significant angular momentum and tilt the spin of the remnant into the collapsing star (Farr et al. 2011a).

Once a black hole is formed, however, changing the spin magnitude is more difficult due to limitations on mass accretion rates affecting how much a black hole can be spun up (Thorne 1974). Once the binary black hole system is formed, the spin magnitudes do not change appreciably over the inspiral (Farr et al. 2014).

No BBH detected to date has a component with confidently high and aligned spin magnitude. The results in the previous section imply that black holes tend to be born with low spin, or that another process (e.g., supernova kicks or dynamical processes involved in binary formation) induces tilts such that $\chi_{\rm eff}$ is small.

The possibility of a spin magnitude distribution that peaks at low spins incurs a degeneracy between models that is not easily overcome: when the spin magnitudes are small enough models produce features which cannot be distinguished within observational uncertainties.

6. DISCUSSION AND CONCLUSIONS

We have presented a variety of estimates for the mass, spin, and redshift distributions of BBH, based on the observed sample of 10 BBH. Some model independent features are evident from the observations. Notably, no binary black holes more massive than GW170729 have been observed to date, but several binaries have component masses likely between $20 - 40 M_\odot$. No highly asymmetric (small q) system has been observed. Only two systems (GW151226 and GW170729) produce a $\chi_{\rm eff}$ distribution which is confidently different from zero; conversely, most BH binaries are consistent with $\chi_{\rm eff}$ near zero. These features drive our inferences about the mass and spin distribution.

Despite exploring a wide range of mass and spin distributions, we find the BBH merger rate density is robustly $R = 52.9^{+55.6}_{-27.0}\,{\rm Gpc}^{-3}\,{\rm yr}^{-1}$. This result is consistent with the fixed model assumptions reported in the combined O1 and O2 observational periods (Abbott et al. 2018). We find a significant reduction in the merger rate for binary black holes with primary masses larger than $\sim 45 M_\odot$.We do not have enough sensitivity to binaries with a black hole mass less than 5 $M_\odot$ to be able to place meaningful constraints on the minimum mass of black holes. We find some evidence that the mass distribution of coalescing black holes may not be a pure power law, instead being slightly better fit by a model including a broad gaussian distribution at high mass. We find the best-fitting models preferentially produce comparable-mass binaries (i.e., $\beta_q > 0$ is preferred).

The mass models in this work supercede results from an older model from O1 which inferred only the power law index (Abbott et al. 2016d, 2017e). That model found systematically larger values of α than its nearest counterpart in this work, Model A, because the older model used a fixed value for the minimum and maximum mass of 5 and 100 $M_\odot$, respectively. This extreme $m_{\rm max}$ is highly disfavored by our current results, and so the older model is also disfavored. Moreover, volumetric sensitivity grows as a strong function of mass. The lack of detections near the older $m_{\rm max}$ drives a preference for a much smaller maximum BH mass in the new models (Fishbach & Holz 2017). A reduced maximum mass is associated with a shallower power-law fit.

We have modeled the spin distribution in several ways, forming inferences on the spin magnitude and tilt distributions. In all of our analysis, the evidence disfavors distributions with large spin components aligned (or nearly aligned) with the orbital angular momentum. We cannot significantly constrain the degree of spin-orbit misalignment in the population. However, regardless of the mass or assumed spin tilt distribution, there is a preference (demonstrated in Figure 7 and Appendix B) for distributions which emphasize lower spin magnitudes. Our inferences suggest 90% of coalescing black hole binaries are formed with $\chi_{\rm eff} < 0.3$. Low spins argue against so-called second generation mergers, where at least one of the components of the binary is a black hole formed from a previous merger (González et al. 2007; Berti et al. 2007) and possesses spins near 0.7 (Fishbach et al. 2017).

Inferring the redshift distribution is difficult with only a small sample of local events (Fishbach et al. 2018). We have constrained models with extreme variation over redshift, favoring instead those which are uniform in the comoving volume or have increasing merger rates with higher redshift. Many potential formation channels in the literature (Belczynski et al. 2014; Rodriguez et al. 2016b; Antonini & Rasio 2016; Mandel & de Mink 2016; Inayoshi et al. 2016; Mapelli et al. 2017; Bartos et al. 2017; Kruckow et al. 2018) produce event rates which are compatible with those from the previous observing runs (Abbott et al. 2018) and this work. It is, of course, plausible that several are contributing simultaneously, and no combination of mass, rate, or redshift dependence explored here rules out any of the channels proposed to date. The next generation of interferometers will allow for an exquisite probe into this dependence at large redshifts (Sathyaprakash et al. 2012; Van Den Broeck 2014; Vitale & Farr 2018).

GW170729 is notable in several ways: it is the most massive, largest $\chi_{\rm eff}$, and most distant redshift event detected so far. To quantify the impact it has on our results, where possible, we have presented model posteriors which reflect its presence in or exclusion from the event set. Many of our predictions are robust despite its extreme values — by far, and not unexpectedly, its influence is most significant in the distribution of $m_{\rm max}$. It also impacts our conclusions about redshift evolution, where its absence flattens the inferred redshift evolution.

Recent modelling using only the first six released events (Wysocki et al. 2018; Roulet & Zaldarriaga 2018) have come to similar conclusions about low spin magnitudes and the shape of the power law distribution. The presence of an apparent upper limit to the merging BBH mass distribution was also observed after the first six released events (Fishbach & Holz 2017). An enhancement which will benefit these types of analyses in the future is a simultaneous fit of the astrophysical model and its parameters and noise background model (Gaebel et al. 2018).

Several studies have noted that population features (Mandel & O'Shaughnessy 2010; Stevenson et al. 2015; Fishbach & Holz 2017; Stevenson et al. 2017a; Zevin et al. 2017; Farr et al. 2017; Talbot & Thrane 2017; Fishbach et al. 2017; Talbot & Thrane 2018; Farr et al. 2018; Barrett et al. 2018; Wysocki et al. 2018) and complementary physics (Abbott et al. 2016f; Zevin et al. 2017; Stevenson et al. 2017a; Chen et al. 2018) will be increasingly accessible as observations accumulate. Given the event merger rates estimated here and anticipated improvements in sensitivity (Abbott et al. 2018), hundreds of BBHs and tens of binary neutron stars are expected to be collected in the operational lifetime of second generation GW instruments. Thus, the inventory of BBH in the coming years will enable inquiries into astrophysics which were previously unobtainable.

REFERENCES

Abbott, B. P., Abbott, R., Abbott, T. D., et al. 2016a, Phys. Rev. Lett., 116, 131103, doi: 10.1103/PhysRevLett.116.131103

—. 2016b, Phys. Rev. Lett., 116, 241103, doi: 10.1103/PhysRevLett.116.241103

—. 2016c, ApJ, 818, L22, doi: 10.3847/2041-8205/818/2/L22

—. 2016d, Physical Review X, 6, 041015, doi: 10.1103/PhysRevX.6.041015

—. 2016e, ApJ, 833, L1, doi: 10.3847/2041-8205/833/1/L1

—. 2016f, Phys. Rev. Lett., 116, 131102, doi: 10.1103/PhysRevLett.116.131102

—. 2017a, ApJ, 851, L35, doi: 10.3847/2041-8213/aa9f0c

—. 2017b, Phys. Rev. Lett., 119, 161101, doi: 10.1103/PhysRevLett.119.161101

—. 2017c, ApJ, 848, L13, doi: 10.3847/2041-8213/aa920c

—. 2017d, Classical and Quantum Gravity, 34, 104002, doi: 10.1088/1361-6382/aa6854

—. 2017e, Phys. Rev. Lett., 118, 221101, doi: 10.1103/PhysRevLett.118.221101

Abbott, B. P., et al. 2018, To be submitted

Abbott, B. P., Abbott, R., Abbott, T. D., et al. 2018, Living Reviews in Relativity, 21, 3, doi: 10.1007/s41114-018-0012-9

Acernese, F., Agathos, M., Agatsuma, K., et al. 2015, Classical and Quantum Gravity, 32, 024001, doi: 10.1088/0264-9381/32/2/024001

Ajith, P., Hannam, M., Husa, S., et al. 2011, Phys. Rev. Lett., 106, 241101, doi: 10.1103/PhysRevLett.106.241101

Alexander, K. D., Berger, E., Fong, W., et al. 2017, ApJ, 848, L21, doi: 10.3847/2041-8213/aa905d

Ali-Haïmoud, Y., Kovetz, E. D., & Kamionkowski, M. 2017, Phys. Rev. D, 96, 123523, doi: 10.1103/PhysRevD.96.123523

Ando, K., Inomata, K., Kawasaki, M., Mukaida, K., & Yanagida, T. T. 2018, Phys. Rev. D, 97, 123512, doi: 10.1103/PhysRevD.97.123512

Antonini, F., Murray, N., & Mikkola, S. 2014, ApJ, 781, 45, doi: 10.1088/0004-637X/781/1/45

Antonini, F., & Perets, H. B. 2012, ApJ, 757, 27, doi: 10.1088/0004-637X/757/1/27

Antonini, F., & Rasio, F. A. 2016, ApJ, 831, 187, doi: 10.3847/0004-637X/831/2/187

Antonini, F., Toonen, S., & Hamers, A. S. 2017, ApJ, 841, 77, doi: 10.3847/1538-4357/aa6f5e

Askar, A., Szkudlarek, M., Gondek-Rosińska, D., Giersz, M., & Bulik, T. 2017, MNRAS, 464, L36, doi: 10.1093/mnrasl/slw177

Babak, S., Taracchini, A., & Buonanno, A. 2017, Phys. Rev. D, 95, 024010, doi: 10.1103/PhysRevD.95.024010

Bai, Y., Barger, V., & Lu, S. 2018, ArXiv e-prints, arXiv:1802.04909. https://arxiv.org/abs/1802.04909

Bailyn, C. D., Jain, R. K., Coppi, P., & Orosz, J. A. 1998, ApJ, 499, 367, doi: 10.1086/305614

Baird, E., Fairhurst, S., Hannam, M., & Murphy, P. 2013, Phys. Rev. D, 87, 024035, doi: 10.1103/PhysRevD.87.024035

Banerjee, S. 2017, MNRAS, 467, 524, doi: 10.1093/mnras/stw3392

Barkat, Z., Rakavy, G., & Sack, N. 1967, Phys. Rev. Lett., 18, 379, doi: 10.1103/PhysRevLett.18.379

Barrett, J. W., Gaebel, S. M., Neijssel, C. J., et al. 2018, MNRAS, 477, 4685, doi: 10.1093/mnras/sty908

Bartos, I., Kocsis, B., Haiman, Z., & Márka, S. 2017, ApJ, 835, 165, doi: 10.3847/1538-4357/835/2/165

Belczynski, K., Bulik, T., Fryer, C. L., et al. 2010, ApJ, 714, 1217, doi: 10.1088/0004-637X/714/2/1217

Belczynski, K., Buonanno, A., Cantiello, M., et al. 2014, ApJ, 789, 120, doi: 10.1088/0004-637X/789/2/120

Belczynski, K., Holz, D. E., Bulik, T., & O'Shaughnessy, R. 2016a, Nature, 534, 512, doi: 10.1038/nature18322

Belczynski, K., Kalogera, V., & Bulik, T. 2002, ApJ, 572, 407, doi: 10.1086/340304

Belczynski, K., Kalogera, V., Rasio, F. A., et al. 2008, The Astrophysical Journal Supplement Series, 174, 223, doi: 10.1086/521026

Belczynski, K., Taam, R. E., Kalogera, V., Rasio, F. A., & Bulik, T. 2007, ApJ, 662, 504, doi: 10.1086/513562

Belczynski, K., Heger, A., Gladysz, W., et al. 2016b, A&A, 594, A97, doi: 10.1051/0004-6361/201628980

Berti, E., Cardoso, V., Gonzalez, J. A., et al. 2007, Phys. Rev. D, 76, 064034, doi: 10.1103/PhysRevD.76.064034

Bethe, H. A., & Brown, G. E. 1998, ApJ, 506, 780, doi: 10.1086/306265

Bird, S., Cholis, I., Mu
textasciitilde noz, J. B., et al. 2016, Phys. Rev. Lett., 116, 201301, doi: 10.1103/PhysRevLett.116.201301

Bond, J. R., Arnett, W. D., & Carr, B. J. 1984, ApJ, 280, 825, doi: 10.1086/162057

Bressan, A., Marigo, P., Girardi, L., et al. 2012, MNRAS, 427, 127, doi: 10.1111/j.1365-2966.2012.21948.x

Carr, B., Kühnel, F., & Sandstad, M. 2016, Phys. Rev. D, 94, 083504, doi: 10.1103/PhysRevD.94.083504

Carr, B. J., & Hawking, S. W. 1974, MNRAS, 168, 399, doi: 10.1093/mnras/168.2.399

Chatterjee, S., Rodriguez, C. L., Kalogera, V., & Rasio, F. A. 2017, ApJ, 836, L26, doi: 10.3847/2041-8213/aa5caa

Chen, H.-Y., Fishbach, M., & Holz, D. E. 2018, Nature, 562, 545, doi: 10.1038/s41586-018-0606-0

Chen, Z.-C., & Huang, Q.-G. 2018, ApJ, 864, 61, doi: 10.3847/1538-4357/aad6e2

Chornock, R., Berger, E., Kasen, D., et al. 2017, ApJ, 848, L19, doi: 10.3847/2041-8213/aa905c

Chruslinska, M., Belczynski, K., Klencki, J., & Benacquista, M. 2018, MNRAS, 474, 2937, doi: 10.1093/mnras/stx2923

Clausen, D., Sigurdsson, S., & Chernoff, D. F. 2013, MNRAS, 428, 3618, doi: 10.1093/mnras/sts295

Coughlin, M., Meyers, P., Thrane, E., Luo, J., & Christensen, N. 2015, Phys. Rev. D, 91, 063004, doi: 10.1103/PhysRevD.91.063004

Coulter, D. A., Foley, R. J., Kilpatrick, C. D., et al. 2017, Science, 358, 1556, doi: 10.1126/science.aap9811

Cowperthwaite, P. S., Berger, E., Villar, V. A., et al. 2017, ApJ, 848, L17, doi: 10.3847/2041-8213/aa8fc7

Damour, T. 2001, Phys. Rev. D, 64, 124013, doi: 10.1103/PhysRevD.64.124013

De Marco, O., Passy, J.-C., Moe, M., et al. 2011, MNRAS, 411, 2277, doi: 10.1111/j.1365-2966.2010.17891.x

de Mink, S. E., Langer, N., Izzard, R. G., Sana, H., & de Koter, A. 2013, ApJ, 764, 166, doi: 10.1088/0004-637X/764/2/166

de Mink, S. E., & Mandel, I. 2016, MNRAS, 460, 3545, doi: 10.1093/mnras/stw1219

Dewi, J. D. M., Podsiadlowski, P., & Sena, A. 2006, MNRAS, 368, 1742, doi: 10.1111/j.1365-2966.2006.10233.x

Dominik, M., Belczynski, K., Fryer, C., et al. 2012, ApJ, 759, 52, doi: 10.1088/0004-637X/759/1/52

—. 2013, ApJ, 779, 72, doi: 10.1088/0004-637X/779/1/72

Dosopoulou, F., & Kalogera, V. 2016, ApJ, 825, 71, doi: 10.3847/0004-637X/825/1/71

Downing, J. M. B., Benacquista, M. J., Giersz, M., & Spurzem, R. 2010, MNRAS, 407, 1946, doi: 10.1111/j.1365-2966.2010.17040.x

—. 2011, MNRAS, 416, 133, doi: 10.1111/j.1365-2966.2011.19023.x

Eldridge, J. J., & Stanway, E. R. 2016, MNRAS, 462, 3302, doi: 10.1093/mnras/stw1772

Ertl, T., Janka, H. T., Woosley, S. E., Sukhbold, T., & Ugliano, M. 2016, ApJ, 818, 124, doi: 10.3847/0004-637X/818/2/124

Farr, B., Holz, D. E., & Farr, W. M. 2018, ApJ, 854, L9, doi: 10.3847/2041-8213/aaaa64

Farr, B., Kalogera, V., & Luijten, E. 2014, Phys. Rev. D, 90, 024014, doi: 10.1103/PhysRevD.90.024014

Farr, W. M., Farr, B., & Littenberg, T. 2015, Modelling Calibration Errors In CBC Waveforms, Tech. Rep. LIGO-T1400682, LIGO Scientific Collaboration and Virgo Collaboration

Farr, W. M., Gair, J. R., Mandel, I., & Cutler, C. 2015, Phys. Rev. D, 91, 023005, doi: 10.1103/PhysRevD.91.023005

Farr, W. M., Kremer, K., Lyutikov, M., & Kalogera, V. 2011a, ApJ, 742, 81, doi: 10.1088/0004-637X/742/2/81

Farr, W. M., Sravan, N., Cantrell, A., et al. 2011b, ApJ, 741, 103, doi: 10.1088/0004-637X/741/2/103

Farr, W. M., Stevenson, S., Miller, M. C., et al. 2017, Nature, 548, 426, doi: 10.1038/nature23453

Finn, L. S., & Chernoff, D. F. 1993, Phys. Rev. D, 47, 2198, doi: 10.1103/PhysRevD.47.2198

Fishbach, M., & Holz, D. E. 2017, ApJ, 851, L25, doi: 10.3847/2041-8213/aa9bf6

Fishbach, M., Holz, D. E., & Farr, B. 2017, ApJ, 840, L24, doi: 10.3847/2041-8213/aa7045

Fishbach, M., Holz, D. E., & Farr, W. M. 2018, ApJ, 863, L41, doi: 10.3847/2041-8213/aad800

Foreman-Mackey, D., Hogg, D. W., & Morton, T. D. 2014, ApJ, 795, 64, doi: 10.1088/0004-637X/795/1/64

Fowler, W. A., & Hoyle, F. 1964, The Astrophysical Journal Supplement Series, 9, 201, doi: 10.1086/190103

Fregeau, J. M. 2004, PhD thesis, MASSACHUSETTS INSTITUTE OF TECHNOLOGY. https://doi.org/10.1063/1.1835214

Freire, P. C. C., Ransom, S. M., Bégin, S., et al. 2008, ApJ, 675, 670, doi: 10.1086/526338

Fryer, C. L., Belczynski, K., Wiktorowicz, G., et al. 2012, ApJ, 749, 91, doi: 10.1088/0004-637X/749/1/91

Fuller, J., Cantiello, M., Lecoanet, D., & Quataert, E. 2015, ApJ, 810, 101, doi: 10.1088/0004-637X/810/2/101

Gaebel, S. M., Veitch, J., Dent, T., & Farr, W. M. 2018, ArXiv e-prints, arXiv:1809.03815. https://arxiv.org/abs/1809.03815

Gelman, A., Carlin, J. B., Stern, H. S., et al. 2004, Bayesian data analysis (Boca Raton, Fla: Chapman & Hall/CRC). https://doi.org/10.1103/PhysRev.136.B1224

Gerosa, D., Berti, E., O'Shaughnessy, R., et al. 2018, Phys. Rev. D, 98, 084036, doi: 10.1103/PhysRevD.98.084036

Gerosa, D., Kesden, M., Sperhake, U., Berti, E., & O'Shaughnessy, R. 2015, Phys. Rev. D, 92, 064016, doi: 10.1103/PhysRevD.92.064016

Giacobbo, N., & Mapelli, M. 2018, MNRAS, 480, 2011, doi: 10.1093/mnras/sty1999

Giacobbo, N., Mapelli, M., & Spera, M. 2018, MNRAS, 474, 2959, doi: 10.1093/mnras/stx2933

Goldstein, A., Veres, P., Burns, E., et al. 2017, ApJ, 848, L14, doi: 10.3847/2041-8213/aa8f41

González, J. A., Sperhake, U., Brügmann, B., Hannam, M., & Husa, S. 2007, Phys. Rev. Lett., 98, 091101, doi: 10.1103/PhysRevLett.98.091101

Gräfener, G., & Hamann, W. R. 2008, A&A, 482, 945, doi: 10.1051/0004-6361:20066176

Grandclément, P., Ihm, M., Kalogera, V., & Belczynski, K. 2004, Phys. Rev. D, 69, 102002, doi: 10.1103/PhysRevD.69.102002

Grindlay, J., Portegies Zwart, S., & McMillan, S. 2006, Nature Physics, 2, 116, doi: 10.1038/nphys214

Hannam, M., Schmidt, P., Bohé, A., et al. 2014, Phys. Rev. Lett., 113, 151101, doi: 10.1103/PhysRevLett.113.151101

Harry, G. M., & LIGO Scientific Collaboration. 2010, Classical and Quantum Gravity, 27, 084006, doi: 10.1088/0264-9381/27/8/084006

Heger, A., Fryer, C. L., Woosley, S. E., Langer, N., & Hartmann, D. H. 2003, ApJ, 591, 288, doi: 10.1086/375341

Heger, A., & Woosley, S. E. 2002, ApJ, 567, 532, doi: 10.1086/338487

Hinder, I., Kidder, L. E., & Pfeiffer, H. P. 2018, Phys. Rev. D, 98, 044015, doi: 10.1103/PhysRevD.98.044015

Hinder, I., Vaishnav, B., Herrmann, F., Shoemaker, D. M., & Laguna, P. 2008, Phys. Rev. D, 77, 081502, doi: 10.1103/PhysRevD.77.081502

Hogg, D. W. 1999, ArXiv e-prints, astro. https://arxiv.org/abs/astro-ph/9905116

Hogg, D. W., Myers, A. D., & Bovy, J. 2010, ApJ, 725, 2166, doi: 10.1088/0004-637X/725/2/2166

Huerta, E. A., Kumar, P., McWilliams, S. T., O'Shaughnessy, R., & Yunes, N. 2014, Phys. Rev. D, 90, 084016, doi: 10.1103/PhysRevD.90.084016

Huerta, E. A., Kumar, P., Agarwal, B., et al. 2017, Phys. Rev. D, 95, 024038, doi: 10.1103/PhysRevD.95.024038

Husa, S., Khan, S., Hannam, M., et al. 2016, Phys. Rev. D, 93, 044006, doi: 10.1103/PhysRevD.93.044006

Inayoshi, K., Kashiyama, K., Visbal, E., & Haiman, Z. 2016, MNRAS, 461, 2722, doi: 10.1093/mnras/stw1431

Inomata, K., Kawasaki, M., Mukaida, K., Tada, Y., & Yanagida, T. T. 2017, Phys. Rev. D, 95, 123510, doi: 10.1103/PhysRevD.95.123510

Ivanova, N., Heinke, C. O., Rasio, F. A., Belczynski, K., & Fregeau, J. M. 2008, MNRAS, 386, 553, doi: 10.1111/j.1365-2966.2008.13064.x

Ivanova, N., Justham, S., Chen, X., et al. 2013, Astronomy and Astrophysics Review, 21, 59, doi: 10.1007/s00159-013-0059-2

Janka, H.-T. 2012, Annual Review of Nuclear and Particle Science, 62, 407, doi: 10.1146/annurev-nucl-102711-094901

Kalogera, V. 2000, ApJ, 541, 319, doi: 10.1086/309400

Khan, S., Husa, S., Hannam, M., et al. 2016, Phys. Rev. D, 93, 044007, doi: 10.1103/PhysRevD.93.044007

Kimpson, T. O., Spera, M., Mapelli, M., & Ziosi, B. M. 2016, MNRAS, 463, 2443, doi: 10.1093/mnras/stw2085

Klein, A., Boetzel, Y., Gopakumar, A., Jetzer, P., & de Vittori, L. 2018, ArXiv e-prints, arXiv:1801.08542. https://arxiv.org/abs/1801.08542

Kovetz, E. D., Cholis, I., Breysse, P. C., & Kamionkowski, M. 2017, Phys. Rev. D, 95, 103010, doi: 10.1103/PhysRevD.95.103010

Kreidberg, L., Bailyn, C. D., Farr, W. M., & Kalogera, V. 2012, ApJ, 757, 36, doi: 10.1088/0004-637X/757/1/36

Kremer, K., Chatterjee, S., Ye, C. S., Rodriguez, C. L., & Rasio, F. A. 2018, ArXiv e-prints, arXiv:1808.02204. https://arxiv.org/abs/1808.02204

Kruckow, M. U., Tauris, T. M., Langer, N., Kramer, M., & Izzard, R. G. 2018, MNRAS, 481, 1908, doi: 10.1093/mnras/sty2190

Kudritzki, R.-P., & Puls, J. 2000, Annual Review of Astronomy and Astrophysics, 38, 613, doi: 10.1146/annurev.astro.38.1.613

Kulkarni, S. R., Hut, P., & McMillan, S. 1993, Nature, 364, 421, doi: 10.1038/364421a0

Langer, N. 2012, Annual Review of Astronomy and Astrophysics, 50, 107, doi: 10.1146/annurev-astro-081811-125534

Littenberg, T. B., Farr, B., Coughlin, S., Kalogera, V., & Holz, D. E. 2015, ApJ, 807, L24, doi: 10.1088/2041-8205/807/2/L24

Loredo, T. J. 2004, in American Institute of Physics Conference Series, ed. R. Fischer, R. Preuss, & U. V. Toussaint, Vol. 735, 195–206. https://doi.org/10.1063/1.1835214

Lower, M. E., Thrane, E., Lasky, P. D., & Smith, R. 2018, Phys. Rev. D, 98, 083028, doi: 10.1103/PhysRevD.98.083028

Madau, P., & Dickinson, M. 2014, Annual Review of Astronomy and Astrophysics, 52, 415, doi: 10.1146/annurev-astro-081811-125615

Maeder, A., & Meynet, G. 2003, A&A, 411, 543, doi: 10.1051/0004-6361:20031491

Mandel, I. 2010, Phys. Rev. D, 81, 084029, doi: 10.1103/PhysRevD.81.084029

Mandel, I., & de Mink, S. E. 2016, MNRAS, 458, 2634, doi: 10.1093/mnras/stw379

Mandel, I., Farr, W. M., Colonna, A., et al. 2017, MNRAS, 465, 3254, doi: 10.1093/mnras/stw2883

Mandel, I., Farr, W. M., & Gair, J. R. 2018, ArXiv e-prints, arXiv:1809.02063. https://arxiv.org/abs/1809.02063

Mandel, I., Haster, C.-J., Dominik, M., & Belczynski, K. 2015, MNRAS, 450, L85, doi: 10.1093/mnrasl/slv054

Mandel, I., & O'Shaughnessy, R. 2010, Classical and Quantum Gravity, 27, 114007, doi: 10.1088/0264-9381/27/11/114007

Mapelli, M. 2016, MNRAS, 459, 3432, doi: 10.1093/mnras/stw869

Mapelli, M., Colpi, M., & Zampieri, L. 2009, MNRAS, 395, L71, doi: 10.1111/j.1745-3933.2009.00645.x

Mapelli, M., & Giacobbo, N. 2018, MNRAS, 479, 4391, doi: 10.1093/mnras/sty1613

Mapelli, M., Giacobbo, N., Ripamonti, E., & Spera, M. 2017, MNRAS, 472, 2422, doi: 10.1093/mnras/stx2123

Marchant, P., Langer, N., Podsiadlowski, P., Tauris, T. M., & Moriya, T. J. 2016, A&A, 588, A50, doi: 10.1051/0004-6361/201628133

Marchant, P., Renzo, M., Farmer, R., et al. 2018, ArXiv e-prints, arXiv:1810.13412. https://arxiv.org/abs/1810.13412

Margalit, B., & Metzger, B. D. 2017, ApJ, 850, L19, doi: 10.3847/2041-8213/aa991c

Margutti, R., Berger, E., Fong, W., et al. 2017, ApJ, 848, L20, doi: 10.3847/2041-8213/aa9057

McKernan, B., Ford, K. E. S., Lyra, W., & Perets, H. B. 2012, MNRAS, 425, 460, doi: 10.1111/j.1365-2966.2012.21486.x

Mennekens, N., & Vanbeveren, D. 2014, A&A, 564, A134, doi: 10.1051/0004-6361/201322198

Messick, C., Blackburn, K., Brady, P., et al. 2017, Phys. Rev. D, 95, 042001, doi: 10.1103/PhysRevD.95.042001

Misner, C. W., Thorne, K. S., & Wheeler, J. A. 1973, Gravitation, first edition edn., Physics Series (San Francisco: W. H. Freeman). https://doi.org/10.1103/PhysRev.136.B1224

Morscher, M., Umbreit, S., Farr, W. M., & Rasio, F. A. 2013, ApJ, 763, L15, doi: 10.1088/2041-8205/763/1/L15

Nicholl, M., Berger, E., Kasen, D., et al. 2017, ApJ, 848, L18, doi: 10.3847/2041-8213/aa9029

Nitz, A. H., Dent, T., Dal Canton, T., Fairhurst, S., & Brown, D. A. 2017, ApJ, 849, 118, doi: 10.3847/1538-4357/aa8f50

Ober, W. W., El Eid, M. F., & Fricke, K. J. 1983, A&A, 119, 61

O'Connor, E., & Ott, C. D. 2011, ApJ, 730, 70, doi: 10.1088/0004-637X/730/2/70

O'Leary, R. M., Rasio, F. A., Fregeau, J. M., Ivanova, N., & O'Shaughnessy, R. 2006, ApJ, 637, 937, doi: 10.1086/498446

O'Shaughnessy, R., Gerosa, D., & Wysocki, D. 2017, Phys. Rev. Lett., 119, 011101, doi: 10.1103/PhysRevLett.119.011101

O'Shaughnessy, R., Kalogera, V., & Belczynski, K. 2010, ApJ, 716, 615, doi: 10.1088/0004-637X/716/1/615

Özel, F., & Freire, P. 2016, Annual Review of Astronomy and Astrophysics, 54, 401, doi: 10.1146/annurev-astro-081915-023322

Özel, F., Psaltis, D., Narayan, R., & McClintock, J. E. 2010, ApJ, 725, 1918, doi: 10.1088/0004-637X/725/2/1918

Özel, F., Psaltis, D., Narayan, R., & Santos Villarreal, A. 2012, ApJ, 757, 55, doi: 10.1088/0004-637X/757/1/55

Packet, W. 1981, A&A, 102, 17

Pan, Y., Buonanno, A., Taracchini, A., et al. 2014, Phys. Rev. D, 89, 084006, doi: 10.1103/PhysRevD.89.084006

Peters, P. C. 1964, Physical Review, 136, 1224, doi: 10.1103/PhysRev.136.B1224

Petrovic, J., Langer, N., & van der Hucht, K. A. 2005, A&A, 435, 1013, doi: 10.1051/0004-6361:20042368

Petrovich, C., & Antonini, F. 2017, ApJ, 846, 146, doi: 10.3847/1538-4357/aa8628

Pian, E., D'Avanzo, P., Benetti, S., et al. 2017, Nature, 551, 67, doi: 10.1038/nature24298

Planck Collaboration, Ade, P. A. R., Aghanim, N., et al. 2016, A&A, 594, A13, doi: 10.1051/0004-6361/201525830

Portegies Zwart, S. F., & McMillan, S. L. W. 2000, ApJ, 528, L17, doi: 10.1086/312422

Portegies Zwart, S. F., McMillan, S. L. W., & Gieles, M. 2010, Annual Review of Astronomy and Astrophysics, 48, 431, doi: 10.1146/annurev-astro-081309-130834

Portegies Zwart, S. F., & Yungelson, L. R. 1998, A&A, 332, 173. https://arxiv.org/abs/astro-ph/9710347

Racine, É. 2008, Phys. Rev. D, 78, 044021, doi: 10.1103/PhysRevD.78.044021

Rodriguez, C. L., & Antonini, F. 2018, ApJ, 863, 7, doi: 10.3847/1538-4357/aacea4

Rodriguez, C. L., Chatterjee, S., & Rasio, F. A. 2016a, Phys. Rev. D, 93, 084029, doi: 10.1103/PhysRevD.93.084029

Rodriguez, C. L., Haster, C.-J., Chatterjee, S., Kalogera, V., & Rasio, F. A. 2016b, ApJ, 824, L8, doi: 10.3847/2041-8205/824/1/L8

Rodriguez, C. L., & Loeb, A. 2018, ApJ, 866, L5, doi: 10.3847/2041-8213/aae377

Rodriguez, C. L., Morscher, M., Pattabiraman, B., et al. 2015, Phys. Rev. Lett., 115, 051101, doi: 10.1103/PhysRevLett.115.051101

Rodriguez, C. L., Zevin, M., Pankow, C., Kalogera, V., & Rasio, F. A. 2016c, ApJ, 832, L2, doi: 10.3847/2041-8205/832/1/L2

Roulet, J., & Zaldarriaga, M. 2018, ArXiv e-prints, arXiv:1806.10610. https://arxiv.org/abs/1806.10610

Sadowski, A., Belczynski, K., Bulik, T., et al. 2008, ApJ, 676, 1162, doi: 10.1086/528932

Sasaki, M., Suyama, T., Tanaka, T., & Yokoyama, S. 2016, Phys. Rev. Lett., 117, 061101, doi: 10.1103/PhysRevLett.117.061101

Sathyaprakash, B., Abernathy, M., Acernese, F., et al. 2012, Classical and Quantum Gravity, 29, 124013, doi: 10.1088/0264-9381/29/12/124013

Savchenko, V., Ferrigno, C., Kuulkers, E., et al. 2017, ApJ, 848, L15, doi: 10.3847/2041-8213/aa8f94

Scheepmaker, R. A., Haas, M. R., Gieles, M., et al. 2007, A&A, 469, 925, doi: 10.1051/0004-6361:20077511

Shu, F. H., & Lubow, S. H. 1981, Annual Review of Astronomy and Astrophysics, 19, 277, doi: 10.1146/annurev.aa.19.090181.001425

Sigurdsson, S., & Hernquist, L. 1993, Nature, 364, 423, doi: 10.1038/364423a0

Skilling, J. 2004, in American Institute of Physics Conference Series, ed. R. Fischer, R. Preuss, & U. V. Toussaint, Vol. 735, 395–405. https://doi.org/10.1063/1.1835238

Soares-Santos, M., Holz, D. E., Annis, J., et al. 2017, ApJ, 848, L16, doi: 10.3847/2041-8213/aa9059

Spera, M., & Mapelli, M. 2017, MNRAS, 470, 4739, doi: 10.1093/mnras/stx1576

Spera, M., Mapelli, M., & Bressan, A. 2015, MNRAS, 451, 4086, doi: 10.1093/mnras/stv1161

Spruit, H. C. 2002, A&A, 381, 923, doi: 10.1051/0004-6361:20011465

Stevenson, S., Berry, C. P. L., & Mandel, I. 2017a, MNRAS, 471, 2801, doi: 10.1093/mnras/stx1764

Stevenson, S., Ohme, F., & Fairhurst, S. 2015, ApJ, 810, 58, doi: 10.1088/0004-637X/810/1/58

Stevenson, S., Vigna-Gómez, A., Mandel, I., et al. 2017b, Nature Communications, 8, 14906, doi: 10.1038/ncomms14906

Stone, N. C., Metzger, B. D., & Haiman, Z. 2017, MNRAS, 464, 946, doi: 10.1093/mnras/stw2260

Sukhbold, T., Ertl, T., Woosley, S. E., Brown, J. M., & Janka, H. T. 2016, ApJ, 821, 38, doi: 10.3847/0004-637X/821/1/38

Talbot, C., & Thrane, E. 2017, Phys. Rev. D, 96, 023012, doi: 10.1103/PhysRevD.96.023012

—. 2018, ApJ, 856, 173, doi: 10.3847/1538-4357/aab34c

Talon, S., & Charbonnel, C. 2005, A&A, 440, 981, doi: 10.1051/0004-6361:20053020

—. 2008, A&A, 482, 597, doi: 10.1051/0004-6361:20078620

Taracchini, A., Buonanno, A., Pan, Y., et al. 2014, Phys. Rev. D, 89, 061502, doi: 10.1103/PhysRevD.89.061502

Tauris, T. M., Kramer, M., Freire, P. C. C., et al. 2017, ApJ, 846, 170, doi: 10.3847/1538-4357/aa7e89

Thorne, K. S. 1974, ApJ, 191, 507, doi: 10.1086/152991

Thorne, K. S. 1983, in Gravitational Radiation, 1–57. https://doi.org/10.1086/162057

Tiwari, V. 2018, Classical and Quantum Gravity, 35, 145009, doi: 10.1088/1361-6382/aac89d

Tiwari, V., Fairhurst, S., & Hannam, M. 2018, ArXiv e-prints, arXiv:1809.01401. https://arxiv.org/abs/1809.01401

Troja, E., Piro, L., van Eerten, H., et al. 2017, Nature, 551, 71, doi: 10.1038/nature24290

Tutukov, A. V., & Yungelson, L. R. 1993, MNRAS, 260, 675, doi: 10.1093/mnras/260.3.675

Ugliano, M., Janka, H.-T., Marek, A., & Arcones, A. 2012, ApJ, 757, 69, doi: 10.1088/0004-637X/757/1/69

Van Den Broeck, C. 2014, in Journal of Physics Conference Series, Vol. 484, 012008. https://doi.org/10.1088/1742-6596/484/1/012008

Veitch, J., Del Pozzo, W., Cody, & Pitkin, M. 2017, johnveitch/cpnest: Minor optimisation, doi: 10.5281/zenodo.835874. https://doi.org/10.5281/zenodo.835874

Veitch, J., Raymond, V., Farr, B., et al. 2015, Phys. Rev. D, 91, 042003, doi: 10.1103/PhysRevD.91.042003

Vink, J. S., & de Koter, A. 2005, A&A, 442, 587, doi: 10.1051/0004-6361:20052862

Vink, J. S., de Koter, A., & Lamers, H. J. G. L. M. 2001, A&A, 369, 574, doi: 10.1051/0004-6361:20010127

Vitale, S., & Farr, W. M. 2018, ArXiv e-prints, arXiv:1808.00901. https://arxiv.org/abs/1808.00901

Vitale, S., Lynch, R., Sturani, R., & Graff, P. 2017, Classical and Quantum Gravity, 34, 03LT01, doi: 10.1088/1361-6382/aa552e

Voss, R., & Tauris, T. M. 2003, MNRAS, 342, 1169, doi: 10.1046/j.1365-8711.2003.06616.x

Woosley, S. E. 2017, ApJ, 836, 244, doi: 10.3847/1538-4357/836/2/244

Woosley, S. E., Blinnikov, S., & Heger, A. 2007, Nature, 450, 390, doi: 10.1038/nature06333

Wysocki, D., Lange, J., & O'Shaughnessy, R. 2018, ArXiv e-prints, arXiv:1805.06442. https://arxiv.org/abs/1805.06442

Wysocki, D., & O'Shaughnessy, R. 2018, Rescaling VT factors to match tabulated VT averages, Tech. Rep. LIGO-T1800427, LIGO Scientific Collaboration and Virgo Collaboration

Zevin, M., Pankow, C., Rodriguez, C. L., et al. 2017, ApJ, 846, 82, doi: 10.3847/1538-4357/aa8408

Ziosi, B. M., Mapelli, M., Branchesi, M., & Tormen, G. 2014, MNRAS, 441, 3703, doi: 10.1093/mnras/stu824

APPENDIX

A. SYSTEMATICS

A.1. *Selection Effects and Sensitive Volume*

The detectability of a BBH merger in GWs depends on the distance and orientation of the binary along with its intrinsic parameters, especially its component masses. In order to model the underlying population and determine the BBH merger rate, we must properly model the mass, redshift and spin-dependent selection effects, and incorporate them into our population analysis according to Equation 11. One way to infer the sensitivity of the detector network to a given population of BBH mergers is by carrying out large scale simulations in which synthetic GW waveforms are injected into the detector data and subsequently searched for. The parameters of the injected waveforms can be drawn directly from the fixed population of interest, or alternatively, the injections can be placed to more broadly cover parameter space and reweighed to match the properties of the population (Tiwari 2018). Such injection campaigns were carried out in Abbott et al. (2018) to measure the total sensitive spacetime volume $\langle VT \rangle$ and the corresponding merger rate for two fixed-parameter populations (power-law and flat-in-log). However, it is computationally expensive to carry out an injection campaign that sufficiently covers the multi-dimensional population hyper-parameter space considered in this work. For this reason, for the parametric population studies in this work, we employ a semi-analytic method to estimate the fraction of found detections as a function of masses, spins and redshift (or equivalently, distance). In this Appendix, we describe our calculations of the network sensitivity, compare it against the results of the injection campaigns in Abbott et al. (2018), and discuss the associated systematic uncertainties.

Our estimates of the network sensitivity are based on the semi-analytic method that was used to infer the BBH mass distribution from the first four GW detections (Abbott et al. 2016d, 2017e). This method assumes that a BBH system is detectable if and only if it produces an SNR $\rho \geq \rho_{\rm th}$ in a single detector, where the threshold SNR, $\rho_{\rm th}$, is typically chosen to be 8. Given a BBH system with known component masses, spins, and cosmological redshift, and a detector with stationary Gaussian noise characterized by a given power spectral density (PSD), one can calculate the optimal SNR, $\rho_{\rm opt}$, of the signal emitted by the BBH merger. The optimal SNR corresponds to the SNR of the signal produced by a face-on, directly overhead BBH merger with the same masses, spins and redshift. Given $\rho_{\rm opt}$, the distribution of single-detector SNRs can be calculated using the analytic distribution of angular factors $\Theta \equiv \rho/\rho_{\rm opt}$ (Finn & Chernoff 1993). Therefore, under these assumptions, the probability of detecting a system of given masses, spins and redshift, $P_{\rm det}(m_1, m_2, \chi_1, \chi_2, z)$, is given by the probability that $\Theta \geq \rho_{\rm th}/\rho_{\rm opt}(m_1, m_2, \chi_1, \chi_2, z)$. $P_{\rm det}$ referred to in this section is equivalent to the $f(z \mid \xi)$ that appears in Equation 12 of Section 2.

The semi-analytic calculation relies on two main simplifying assumptions: the detection threshold $\rho_{\rm th}$, and the choice of PSD for characterizing the detector noise. When fitting the mass distribution to the first four BBH events in Abbott et al. (2017e), we assumed that the PSD in each LIGO interferometer could be approximated by the Early High Sensitivity curve in Abbott et al. (2018) during O1 and the first few months of O2, and we fixed $\rho_{\rm th} = 8$. We refer to the sensitivity estimate under these assumptions as the raw semi-analytic calculation. In reality, the detector PSD fluctuates throughout the observing period. Additionally, the fixed detection threshold on SNR does not directly account for the empirical distributions of astrophysical and noise triggers, and does not have a direct correspondence with the detection statistic used by the GW searches to rank signifiance of triggers (Nitz et al. 2017; Messick et al. 2017; Abbott et al. 2018). Consequently, the sensitive spacetime volume of a population estimated using an SNR threshold may differ from the one obtained using injections, which threshold on the pipeline-dependent detection statistic. We therefore pursue two modifications to the raw semi-analytic calculation in order to ensure that our sensitivity estimates and the resulting population estimates remain unbiased. In the first modification, which we employ throughout the mass distribution analysis (Section 3), we calibrate the raw semi-analytic method to the injection campaign in Abbott et al. (2018). The calibration takes the form of mass-dependent calibration factors, calculated according to Wysocki & O'Shaughnessy (2018). Compared to the raw semi-analytic calculation, using the calibrated sensitive volume in the mass-distribution analysis has a small effect on the inferred shape of the mass distribution and a slightly more noticeable effect on the inferred rates (see the discussion in the following subsection).

An alternative modification of the semi-analytic method, which we pursue in the redshift evolution analysis, is to approximate the PSD as constant in 30, five-day chunks of analysis time over O1 and O2, rather than using a fixed PSD for all of O1 and O2. For this method, the 30 PSDs are calculated for the Livingston detector (L1), as we find that this matches the redshift-dependent sensitivity empirically determined by the injection campaigns (see Figure 10).

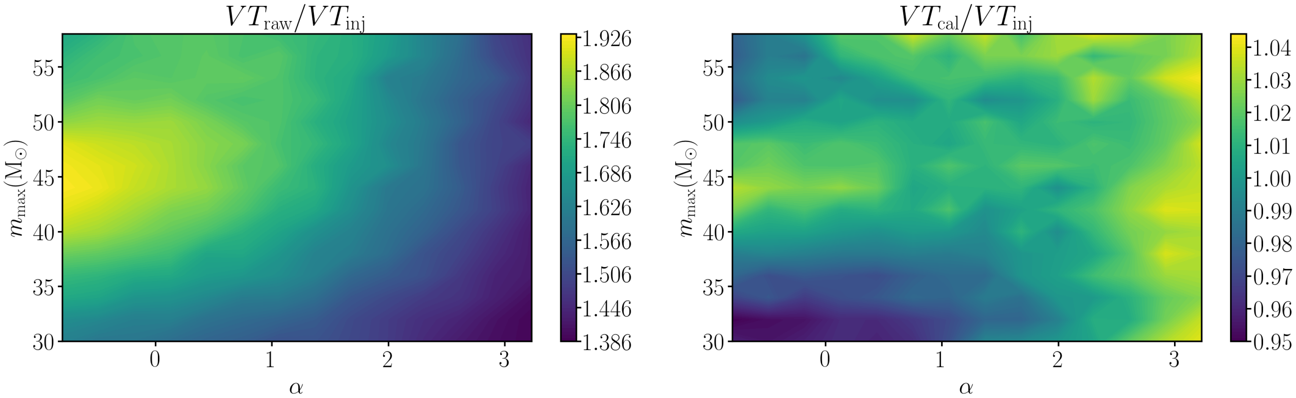

Figure 9. Ratio between the raw semi-analytic computation of $\langle VT \rangle$ to the $\langle VT \rangle$ computed by injections into the search pipeline (left panel), and the same ratio for the mass-calibrated $\langle VT \rangle$ (right panel), for different mass distributions described by the two-parameter Model A. The $\langle VT \rangle$ for the injections are calculated for a threshold of $\varrho = 8.0$, where ϱ is the signal-noise model statistic used in the PyCBC analysis of O2 data. This threshold roughly matches the detection statistic of the lowest significance detection, GW170729, which has $\varrho = 8.7$ in PyCBC. We use the mass-calibrated $\langle VT \rangle$ for the parametric mass- and spin-distribution analyses in Section 3 and 5 in order to better match the injection results. However, the difference between all three methods is small compared to our statistical uncertainty in the mass distribution, particularly where posterior support for the mass distribution hyper-parameters is high, indicating that systematic uncertainties in the $\langle VT \rangle$ estimation do not have a large impact on our results.

Replacing the constant PSD with a time-varying PSD also has a small effect on the inferred mass distribution, but is important in accurately capturing the redshift-dependent detection probability, especially at high redshifts, because the detection horizon fluctuates with time.

For the analyses in this work, we find that including first-order spin effects in the calculation of $P_{\rm det}$ and the corresponding sensitive spacetime volume $\langle VT \rangle$ results in nearly indistinguishable population estimates compared to neglecting spin entirely. For this reason, in the text we freely mix results which use spin-dependent $\langle VT \rangle$ and spin-independent $\langle VT \rangle$ estimates. In the following subsection, we detail the comparisons between the semi-analytic calculations and the results of the injection campaigns, and discuss remaining systematic uncertainties.

A.2. *Semi-Analytic Sensitivity Models versus Injections*

The semi-analytic calculation yields an estimate of the detection probability $P_{\rm det}(m_1, m_2, \chi_1, \chi_2, z)$, or equivalently:

$$P_{\rm det}(\theta) = \int p(\xi, z \mid \theta) P_{\rm det}(\xi, z) \mathrm{d}\xi \mathrm{d}z, \tag{A1}$$

where θ are the population hyperparameters and ξ are the intrinsic parameters of the system. (We assume sources are distributed uniformly on the sky with isotropic orientations.) The detection probability and the corresponding sensitive spacetime volume of a given population described by hyperparameters θ can be empirically calculated for a few fixed values of θ via a Monte-Carlo injection campaign (Abbott et al. 2018) as described above. When calculating $\langle VT \rangle$ from injections into the PyCBC detection pipeline, we consider injections to be "detected" if they have a detection statistic $\varrho \geq 8$, where ϱ is the statistic used in the PyCBC analysis of O2 data (Nitz et al. 2017; Abbott et al. 2018). This is comparable to the detection statistic $\varrho = 8.7$ of the lowest-significance GW event included in our analysis, GW170729. As discussed in Section 4, because we adopt a fixed detection threshold, our analysis differs from the rate analysis in Abbott et al. (2018), which does not fix a detection threshold, instead assigning to each trigger a probability of astrophysical origin (Farr et al. 2015). We compare the injection-determined $\langle VT \rangle$ to the semi-analytic calculation for a few fixed choices of θ in order to calculate mass-dependent calibration factors. We then use these factors to calibrate the semi-analytic results (Wysocki & O'Shaughnessy 2018). Figure 9 shows the comparison between the raw semi-analytic $\langle VT \rangle$, the calibrated $\langle VT \rangle$, and the injection $\langle VT \rangle$ across the two-dimensional hyperparameter space of Model A for the mass distribution. We have repeated our mass distribution analysis with different choices of the $\langle VT \rangle$ calibration, and found that the effect on the shape of the mass distribution and the overall merger rate $\mathcal{R}$ are much smaller than the differences between Models A, B and C and the statistical errors associated with a small sample of 10

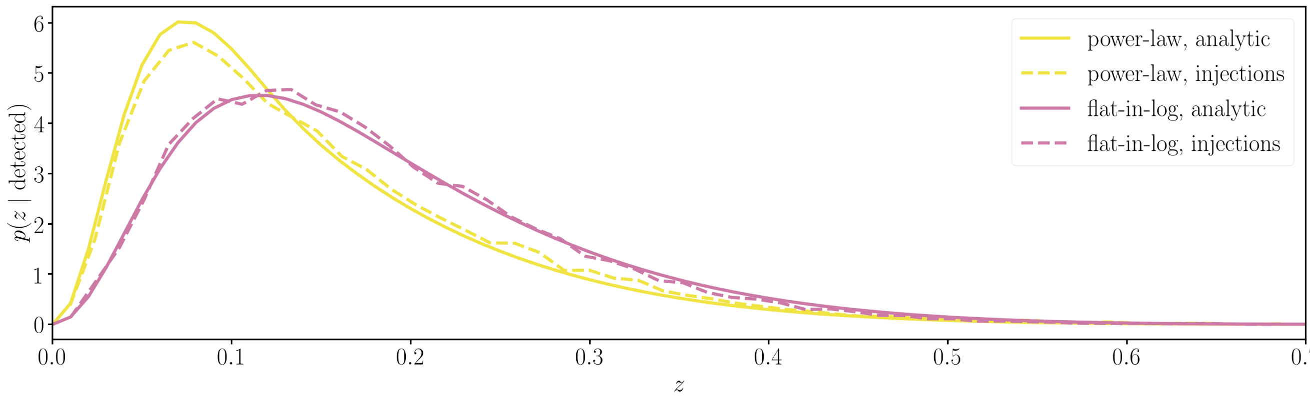

Figure 10. Redshift distribution of injections recovered with a false alarm rate (FAR) less than 0.1 yr^{-1} by the search pipeline GstLAL for the two fixed-parameter injection sets, power-law (red) and flat-in-log (green) compared to the expectation from the semi-analytic calculation used for the redshift evolution analysis, as described in the text. The underlying redshift distribution of the injected populations are assumed to follow a uniform in comoving volume and source-frame time distribution. The FAR threshold of 0.1 / year nearly matches the FAR of the lowest-significance GW event, GW170729, with a FAR of 0.18 / year in the GstLAL pipeline. The semi-analytic calculation closely predicts the redshift distribution of the found injections.

events. We have also investigated whether simply omitting all spin dependence from the $\langle VT \rangle$ calculation appreciably changed our results for the joint mass distribution – merger rate inference. Except for an overall scale factor easily absorbed into our calibration, we find even this extreme choice for $\langle VT \rangle$ does not significantly change our results. Therefore, the systematic uncertainties associated with different choices for calculating the mass- and spin-dependent selection effects do not affect our conclusions regarding the mass and spin distributions and the merger rate.

For the redshift evolution analysis (Section 4), it is not sufficient to calibrate the mass-dependence of the detection probability; we must verify that the semi-analytic calculation reproduces the proper redshift-dependence. We achieve this by accounting for the fluctuating detector sensitivity and replacing the single PSD of the raw semi-analytic calculation with a different PSD calculated for the Livingston detector for each five-day chunk of observing time. We find that this assumption correctly reproduces the redshift distribution of found injections, as shown in Figure 10. Adopting different assumptions, such as using the PSDs calculated for the Hanford detector instead of the Livingston detector, or changing the single-detector SNR threshold away from 8, yields curves in Figure 10 that deviate significantly from the distribution of recovered injections. We note that although we use a different variation of the semi-analytic $\langle VT \rangle$ calculation for the redshift evolution analysis, the relative difference in the total $\langle VT \rangle$, is less than 10% compared to the raw semi-analytic calculation over the range of mass distributions with posterior support.

An additional systematic uncertainty we have neglected in the $\langle VT \rangle$ and parametric rates calculations is the calibration uncertainty. While the event posterior samples have incorporated a marginalization over uncertainties on the calibration Farr et al. (2015) for both strain amplitude and phase, the $\langle VT \rangle$ estimation here does not. The amplitude calibration uncertainty results in an 18% volume uncertainty (Abbott et al. 2018), which is currently below the level of statistical uncertainty in our population-averaged merger rate estimate.

A.3. *Waveform systematics*

Another potential source of bias is the choice of waveform family used to calculate $\langle VT \rangle$ as well as the parameters of individual events. While the two predominantly used waveform families `SEOBNRv3` (Pan et al. 2014; Babak et al. 2017) and `IMRPhenomPv2` (Hannam et al. 2014; Khan et al. 2016; Husa et al. 2016) both capture a wide variety of physical effects including simple precession and other spin effects, they do not match exactly over the whole of the parameters space. For the $\langle VT \rangle$ estimation, differences between the phasing, and more importantly, the amplitude of the waveform can lead to different SNRs and detection statistics for the same sets of physical parameters. We carry out the injection-based $\langle VT \rangle$ estimation for both waveforms and find that for populations described by the two-parameter mass Model A, the waveforms produce $\langle VT \rangle$ estimates consistent to 10% across the relevant region of hyperparameter space with high posterior probability. Therefore, compared to the statistical uncertainties, the choice is waveform does not contribute a significant systematic uncertainty for the $\langle VT \rangle$ estimation.

Our choice of waveform model also propagates into our inferences about each event, and hence nominally into the population inferences, particularly the distributions of mass ratio and spin. To directly assess the impact of these uncertainties on our results, we have repeated several of our calculations (for parametric rate distributions) with different inferences about two key events (GW170729 and GW151226) obtained via `SEOBNRv3`. We find that this waveform model produces at most modestly different inferences about key parameters. For example, this modification of the standard Model B analysis predicts the 90% upper bound of a_1 to be 0.7 and credible intervals on $m_{\max}$ and $\mathcal{R}$ to be $36.6 - 51.7 M_{\odot}$ and $25.7 - 109.6\,\mathrm{Gpc}^{-3}\,\mathrm{yr}^{-1}$, which is consistent with our standard Model B estimates of 0.7, $36.3 - 56.9 M_{\odot}$, and $24.4 - 111.7\,\mathrm{Gpc}^{-3}\,\mathrm{yr}^{-1}$. We again find largely unchanged results for the population.

B. ALTERNATIVE SPIN MODELS

B.1. *Spin Models*

In addition to the approaches in Section 5, we perform here a number of complementary analyses to reinforce our results.

B.2. *Model Selection*

We choose a set of specific realizations of the general model described in Section 2.2, building on Farr et al. (2017); Tiwari et al. (2018). For the spin magnitude we consider four discrete models, the first three being special cases of Equation 4:

- Low (L): $p(a) = 2(1 - a)$, i.e., $\alpha_a = 1$, $\beta_a = 2$.
- Flat (F): $p(a) = 1$, i.e., $\alpha_a = 1$, $\beta_a = 1$.
- High (H): $p(a) = 2a$, i.e., $\alpha_a = 2$, $\beta_a = 1$.
- Very low (V): $p(a) \propto \exp -(a/0.2)$

Such magnitude distributions are chosen as simple representations of low, moderate and highly spinning individual black holes. The very low (V) population is added to capture the features of an even lower spinning population — this is motivated by the features at low spin of the parametric distribution featured in Figure 7.

For spin orientations we consider three fixed models representing extreme cases of Equation 6:

- Isotropic (I): $p(\cos t_i) = 1/2$; $-1 < \cos t_i < 1$, i.e., $\zeta = 0$.
- Aligned (A): $p(\cos t_i) = \delta(\cos t_i - 1)$, i.e., $\zeta = 1$, $\sigma_i = 0$.
- Restricted (R): $p(\cos t_i) = 1$; $0 < \cos t_i < 1$, this is the same as I, except the spins are restricted to point above the orbital plane.

The isotropic distribution is motivated by dynamical or similarly disordered assembly scenarios. The aligned distribution is motivated by formation in an isolated binary, under the simplifying assumption that the stars remain perfectly aligned throughout their evolution. The restricted model R is only used to generate $\chi_{\rm eff}$ distributions which are positive but otherwise retain the same shape as a similar isotropic distribution I. Comparing pairs of restricted and isotropic models to the data provides another way to query whether our data favors binaries with $\chi_{\rm eff} > 0$ or not. While we have mathematically defined the R model by assuming tilted spins, the same $\chi_{\rm eff}$ distribution as an R model can be generated with nonprecessing spins.

Figure 11 illustrates the $\chi_{\rm eff}$ distributions implied by each of these scenarios. Following Farr et al. (2017); Tiwari et al. (2018), we calculate the evidence and compute the Bayes factors for the 12 different scenarios outlined above. Since the $\chi_{\rm eff}$ distribution also depends on the distribution of masses, the Bayes factors are computed for three different mass distributions. Two of these fix the mass ratio to fiducial values, $q = 1$ and $q = 0.5$. The third corresponds to a fixed parameter model with $\alpha = 1, m_{\min} = 5, m_{\max} = 50$.

Table 6, shows the log Bayes factors for each of the zero-dimensional spin models described in Section 2. The Bayes factors use the low and isotropic distribution (LI) as the reference. Because of degeneracies in the GW waveform between mass ratio and $\chi_{\rm eff}$, the choice of mass distribution impacts inferences about spins. This effect explains the significant difference in Bayes factors for the third row in the table. We find again our result moderately favors small

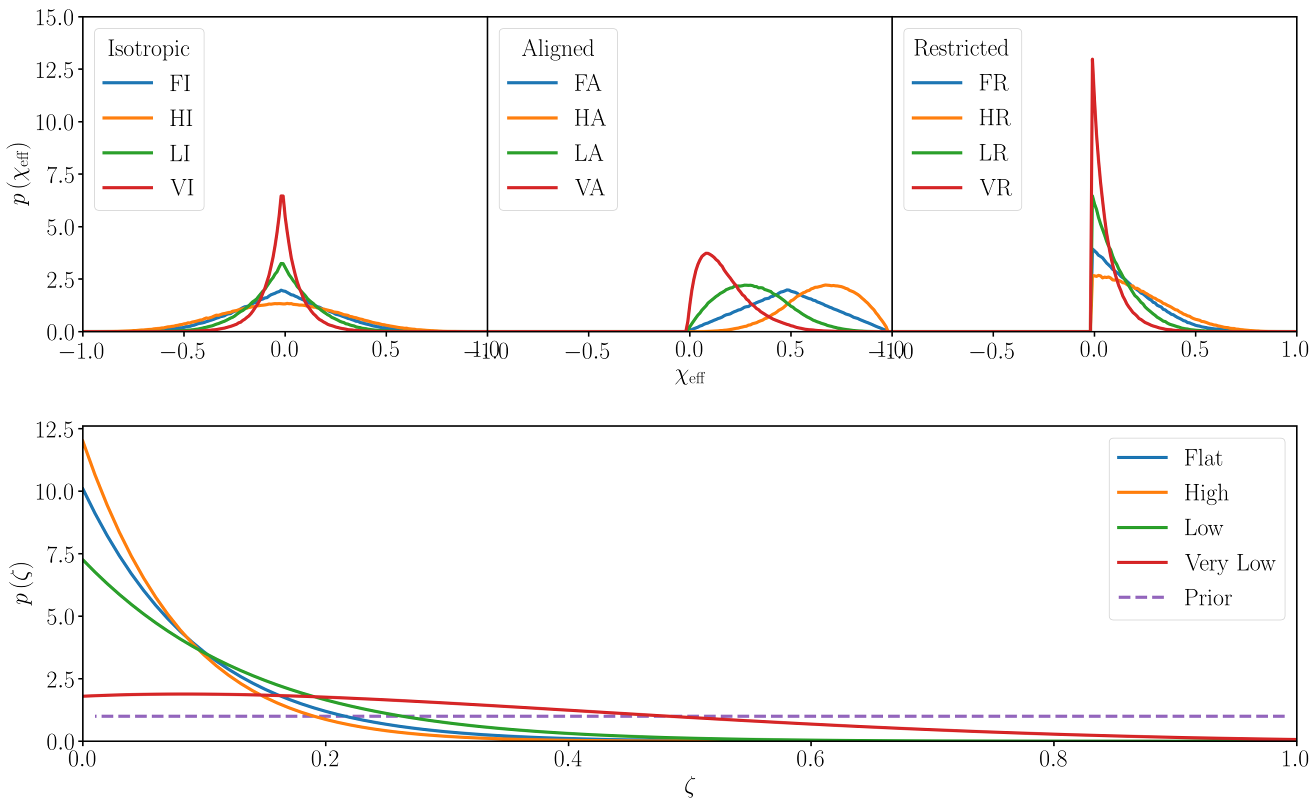

Figure 11. Upper row: $p(\chi_{\rm eff})$ under various model assumptions. Labels in each subpanel legend correspond to the tilt and magnitude models defined in B.2. Isotropic models (left) provide support for both negative and positive $\chi_{\rm eff}$. Aligned models (center) assume perfect alignment for each of the four magnitudes distributions. Restricted models (right) have the same shape as the Isotropic ones, with support over $\chi_{\rm eff} > 0$ only. However they can be generated with nonprecessing spins. Bottom row: Posterior on the mixture fraction ζ between isotropic and aligned distributions. $\zeta = 0$ corresponds to a completely isotropic distribution.

$q = 1$	Very low	Low	Flat	High
Isotropic	1.10	0.0	-0.93	-2.07
Restricted	3.39	3.26	1.31	0.11
Aligned	1.58	-4.12	-12.92	-32.37
$q = 0.5$	Very low	Low	Flat	High
Isotropic	1.14	0.0	-1.03	-2.41
Restricted	3.45	3.26	1.23	-0.25
Aligned	1.69	-3.71	-12.22	-30.73
fixed param.	Very low	Low	Flat	High
Isotropic	1.40	0.0	-2.63	-4.61
Restricted	1.76	0.11	-2.78	-4.88
Aligned	-3.78	-14.45	-24.28	-48.00

Table 6. Natural log Bayes factors for various spin distributions. The orientation models are described in Section 2. We find modest evidence for small spins. When spins are small, we cannot make strong statements about the distribution of spin orientations.

black hole spins. The restricted models with $\chi_{\rm eff}$ strictly positive consistently produce the highest Bayes factors. For the small-spin magnitude models we cannot make strong statements about the distribution of spin orientations. Models containing highly spinning components are significantly disfavored, with high or flat aligned spins particularly selected against (e.g., FA and HA are disfavored with Bayes factors ranging in $\left[10^{-11}, 10^{-6}\right]$ and $\left[10^{-21}, 10^{-13}\right]$, respectively). As a bracket for our uncertainty on the mass and mass ratio distribution, we evaluated the Bayes factors for the fixed parameter model $\alpha = 2.3$, $m_{\rm min} = 5$, $m_{\rm max} = 50$. They differ from the third mass model in Table 6 by a factor comparable to unity.

B.3. *Spin Mixture Models*

The models considered for model selection in Table 6 all assume a fixed set of spin magnitudes and tilts. There is no reason to believe, however, that the Universe produces from only one of these distributions. A natural extension is to allow for a mixing fraction describing the relative abundances of perfectly-aligned and isotropically distributed black holes spins. We assume that the aligned and isotropic components follow the same spin magnitude distribution. It is possible that black holes with a different distribution of spin orientations would have a different distribution of spin magnitudes, but given our weaker constraints on spin magnitudes, we focus on spin tilts sharing the same magnitude distribution.

We compute the posterior on the fraction of aligned binaries ζ in the population as per Equation 6 in the limit $(\sigma_i \to 0)$. The models here are subsets of the Mixture distribution, with a purely isotropic being $\zeta = 0$, and completely aligned being $\zeta = 1$. The prior on the mixing fraction is flat.

All of the models which contain a completely aligned component favor isotropy over alignment. This ability to distinguish a mixing fraction diminishes with smaller spin magnitudes. This is because such spin magnitudes yield populations which are not distinguishable to within measurement uncertainty of $\chi_{\rm eff}$. We do not include the most-favored restricted (R) configuration, but expect that the results would be similar. Coupled with the model selection results in the previous section, this implies that the mixing fraction is not well determined when fixed to the models (low and very low) which are favored by the data (see Figure 11). As stated above, in this case our ability to measure the mixing fraction is negligible.

B.4. *Three-bin Analysis of $\chi_{\rm eff}$*

We illustrate here how $\chi_{\rm eff}$ measurements can provide insights into discerning spin orientation distributions. Following Farr et al. (2018), we split the range of $\chi_{\rm eff}$ into three bins. One encompasses the fraction of uninformative binaries with $\chi_{\rm eff}$ consistent with zero ($|\chi_{\rm eff}| \leq 0.05$); the vertical axis of Figure 12 shows the fraction of binaries lying outside of this bin. The other two capture significantly positive ($\chi_{\rm eff} > 0.05$), and significantly negative ($\chi_{\rm eff} < -0.05$) binaries. The width 0.05 is chosen to be of the order of the uncertainty in a typical event posterior.

The aligned spin scenario is preferred in the posterior support on the right half of Figure 12: the small fraction of binaries which are informative tend to possess $\chi_{\rm eff}$ greater than zero. Conversely, if the spins are isotropic, there would be no preference for positive or negative $\chi_{\rm eff}$, and the posterior in Figure 12 would peak towards the middle. However, of the ten observed binaries, eight are consistent with zero $\chi_{\rm eff}$ and only two are informative, thus demonstrating our ability to distinguish between the two scenarios is weak.

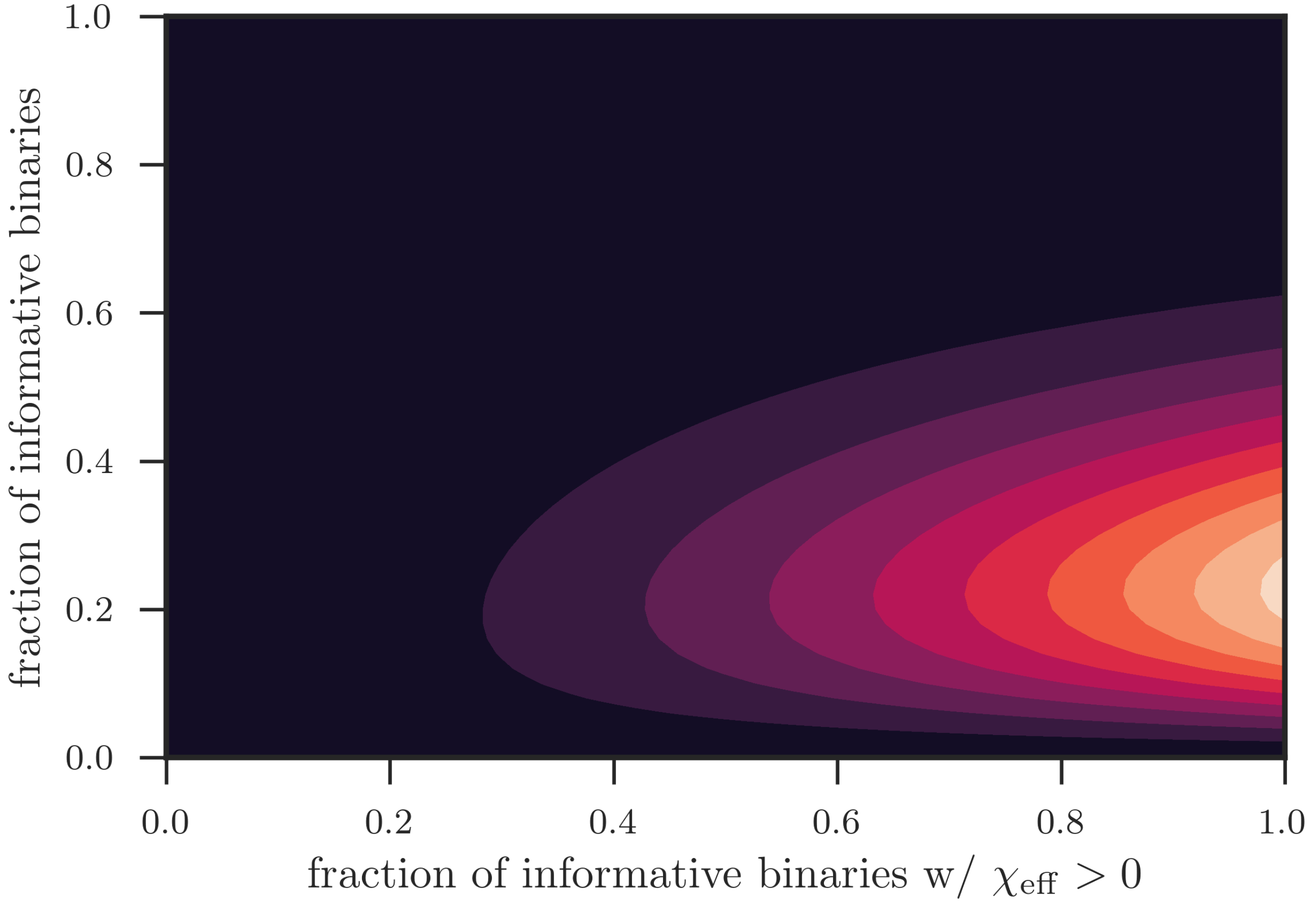

Figure 12. Posterior distribution for the fraction of informative binaries (i.e., $|\chi_{\rm eff}| > 0.05$), and the fraction of those informative binaries with positive $\chi_{\rm eff}$ (i.e., $\chi_{\rm eff} > 0.05$).